

A New Measurement of the Stellar Mass Density at $z \simeq 5$: Implications for the Sources of Cosmic Reionization

D. P. Stark ¹, A. J. Bunker ², R. S. Ellis ¹, L. P. Eyles ², M. Lacy ³

ABSTRACT

We present a new measurement of the integrated stellar mass per comoving volume at redshift 5 determined via spectral energy fitting drawn from a sample of 214 photometrically-selected galaxies with $z'_{850LP} < 26.5$ in the southern GOODS field. Following procedures introduced by Eyles et al. (2005), we estimate stellar masses for various sub-samples for which reliable and unconfused Spitzer IRAC detections are available. A spectroscopic sample of 14 of the most luminous sources with $\bar{z} = 4.92$ provides a firm lower limit to the stellar mass density of $1 \times 10^6 M_{\odot} \text{ Mpc}^{-3}$. Several galaxies in this sub-sample have masses of order $10^{11} M_{\odot}$ implying significant earlier activity occurred in massive systems. We then consider a larger sample whose photometric redshifts in the publicly-available GOODS-MUSIC catalog lie in the range $4.4 < z < 5.6$. Before adopting the GOODS-MUSIC photometric redshifts, we check the accuracy of their photometry and explore the possibility of contamination by low- z galaxies and low-mass stars. After excising probable stellar contaminants and using the $z'_{850LP} - J$ color to exclude any remaining foreground red galaxies, we conclude that 196 sources are likely to be at $z \simeq 5$. The implied mass density from the unconfused IRAC fraction of this sample, scaled to the total available, is $6 \times 10^6 M_{\odot} \text{ Mpc}^{-3}$. We discuss the uncertainties as well as the likelihood that we have underestimated the true mass density. Including fainter and quiescent sources the total integrated density could be as high as $1 \times 10^7 M_{\odot} \text{ Mpc}^{-3}$. Even accounting for 25% cosmic variance within a single GOODS field, such a high mass density only 1.2 Gyr after the Big Bang has interesting consequences for the implied past average star formation during the period when cosmic reionization is now thought to have taken place. Using the currently available (but

¹Department of Astronomy, California Institute of Technology, MS 105-24, Pasadena, CA 91125; dps@astro.caltech.edu

²School of Physics, University of Exeter, Stocker Road, Exeter EX4 4QL, U.K.

³Spitzer Science Center, California Institute of Technology, MC-220-6, 1200 E. California Blvd, Pasadena, CA 91125, U.S.A.

highly uncertain) rate of decline in the star formation history over $5 < z < 10$, a better fit is obtained for the assembled mass at $z \simeq 5$ if we admit significant dust extinction at early times or extend the luminosity function to very faint limits. An interesting consequence of the latter possibility is an abundant population of low luminosity sources just beyond the detection limits of current surveys. As mass density estimates improve at $z \simeq 5$ -6, our method is likely to provide one of the tightest constraints on the question of whether star forming sources were responsible for reionizing the Universe.

Subject headings: galaxies: formation – galaxies: evolution – galaxies: starburst – galaxies: high redshift – ultraviolet: galaxies – surveys

1. Introduction

Finding the sources responsible for cosmic reionization is now the active frontier in studies of galaxy formation. A number of independent arguments are focusing efforts on searches for star forming galaxies in the redshift interval $5 < z < 10$. Studies of the optical depth in Lyman α absorption probed by high resolution spectra of the most distant quasars suggest an upward transition in the neutral fraction beyond $z \simeq 5.5$ (Fan et al. 2006); these data suggest reionization was just ending at $z \simeq 6$. In contrast, the optical depth of microwave photons to electron scattering derived from the angular power spectrum of the WMAP polarization-temperature cross-correlation function (Spergel et al. 2006) places a valuable upper bound on the reionization process corresponding to $z \simeq 10$ -20.

Over the past several years, the quest to observe the most distant galaxies in the Universe has rapidly expanded to the point where the discovery of $z \simeq 5 - 6$ star-forming galaxies has now become routine. Deep imaging surveys with the *Hubble Space Telescope (HST)* and 8-10 meter ground based telescopes have uncovered hundreds of galaxies at $z \simeq 5$ (Iwata et al. 2003; Bremer et al. 2004) and $z \simeq 6$ (Bunker et al. 2004; Dickinson et al. 2004; Bouwens et al. 2006) via the Lyman break galaxy (LBG) technique pioneered by Steidel and collaborators to identify star-forming galaxies at $z \approx 3 - 4$ (Steidel et al. 1996, 1999).

The consensus emerging from these studies, however, is that abundance of *luminous* galaxies is substantially *less* at $z \approx 6$ than at $z \approx 3$ (Stanway et al. 2003; Bunker et al. 2004; Dickinson et al. 2004; Bouwens et al. 2006). If this trend continues to fainter systems and higher redshift, then it may prove challenging to explain the earlier star formation activity necessary to fulfill reionization in the redshift interval $5 < z < 10$ implied by the quasar and WMAP studies (Bunker et al. 2004). However, it has been suggested that the evolution in

the galaxy luminosity function between $z = 3$ and $z = 6$ is luminosity dependent: although the entire luminosity function is not yet well-constrained at $z \approx 6$, intrinsically fainter galaxies appear to become more abundant at earlier times (Bouwens et al. 2006). If this is the case, then the bulk of reionizing photons could come from lower luminosity galaxies not yet adequately probed in deep surveys.

As the redshift boundary of cosmic reionization narrows, so it becomes crucial to improve our understanding of the cosmic star formation history in the corresponding time interval. Unfortunately however, confirming even the most luminous sources in the range $7 < z < 10$ is challenging for current facilities. Although some candidate $z \simeq 7 - 10$ galaxies have been identified in ACS and lensed surveys (Bouwens et al 2004b, Bouwens et al 2005, Richard et al 2006, Stark et al. 2007), these are generally too faint for spectroscopic study. The situation may not significantly improve for several years.

This paper explores a more practical approach for constraining the amount of star formation prior to $z \simeq 5-6$, namely the measurement of the integrated stellar mass density at this epoch. Following the idea originally discussed by Stark & Ellis (2006), the stellar mass density at $z \simeq 5-6$ must represent the integral of past activity. With adequate precision, such estimates can be used to independently verify the claimed decline in overall star formation to $z \simeq 10$ and to assess whether the past activity is sufficient for cosmic reionization.

The approach is made practical by the remarkable progress recently made in estimating stellar masses at high redshift via the use of the Infrared Array Camera (IRAC, Fazio et al. 2004) onboard the *Spitzer Space Telescope*. Egami et al. (2005) first demonstrated the technique for one of the most distant known sources: a multiply-imaged pair with a photometric redshift of $z \simeq 6.8$. Eyles et al. (2005) later extended the technique for two spectroscopically-confirmed galaxies at $z = 5.8$, demonstrating the presence of massive galaxies ($M_{\text{stellar}} > 10^{10} M_{\odot}$) with evolved stellar populations of ages $\gg 100$ Myr.

The IRAC filters at $3.6 - 8.0 \mu\text{m}$ probe the rest-frame optical at $z \approx 5 - 6$, providing a valuable indicator of established stellar populations and, indirectly, hinting at vigorous star formation activity at $z > 6$. Combining these data with deep broadband optical photometry from *HST* and 8-10 meter class ground based telescopes, spectral energy distributions (SEDs) can be compared with population synthesis models to constrain the age, star formation history and stellar masses of galaxies. The initial discovery of massive ($10^{10} M_{\odot}$) galaxies at $z \simeq 6$ presented in Eyles et al. (2005) was subsequently confirmed by the independent analysis of Yan et al. (2005). More recently, Mobasher et al. (2005) identified a galaxy in the Hubble Ultra Deep Field (UDF) with a photometric redshift of $z \simeq 6.5$ (but see also the recent paper by Dunlop et al. 2006). If this high redshift is correct, then the MIPS and IRAC detections imply a very massive system of $M_{\text{stellar}} > 10^{11} M_{\odot}$, providing further

evidence for significant star formation activity at $z > 6$ (Panagia et al. 2005).

The studies of galaxy masses published thus far have focused on only a few individual systems. Although some studies (e.g. Stark & Ellis 2006) have attempted to infer the contribution of past star formation to cosmic reionization, without knowing how typical such massive galaxies are, it is difficult to make precise statements. Clearly what is needed is a *census* of the assembled stellar mass at high redshift. A comoving *stellar mass density* can be directly compared with various models of earlier star formation.

In a companion paper, we compute the stellar mass density at $z \approx 6$ from the i' -band dropouts in GOODS-South (Eyles et al. 2006). A similar study of i' -drops was conducted in Yan et al. (2006). However, the surface density of i' -band dropout galaxies at $z \approx 6$ with *Spitzer* detections is low. A more statistically-meaningful sample can be found using the $z \approx 5$ v -band dropouts. The age of the Universe at this time is only marginally older (1.2 Gyr c.f. 0.95 Gyr) yet larger, more representative, samples are available. In this paper we will examine the stellar mass density at $z \approx 5$ using sources to a limiting magnitude of $z'_{850LP} \approx 26.5$ selected from the Great Observatories Origins Deep Survey (GOODS, Giavalisco et al. 2004b). We present an analysis of various subsamples at $z \approx 5$ drawn from a total of $\simeq 214$ v -band dropouts. The goal of the study is to establish whether the assembled stellar mass at $z \simeq 5$ is consistent with current (and admittedly uncertain) estimates of the preceding star formation activity. If not, this might be taken to imply a significant component of star formation is missing, occurring either at lower intrinsic luminosities, obscured by dust, or at uncharted epochs ($z > 10$).

A plan of the paper follows. In §2, §3, and §4, we introduce the various imaging and spectroscopic datasets, the photometric procedures and the selection of various subsamples of $z \simeq 5$ galaxies. We describe the derivation of the stellar masses and comment on the uncertainties in §5. In §6, we examine the implications for the star formation history at earlier times.

We adopt a cosmology consistent with the initial WMAP data release (Spergel et al. 2003): a Λ -dominated, flat universe with $\Omega_\Lambda = 0.7$, $\Omega_M = 0.3$ and $H_0 = 70 h_{70} \text{ km s}^{-1} \text{ Mpc}^{-1}$. All magnitudes in this paper are quoted in the AB system (Oke & Gunn 1983).

2. The GOODS-S Dataset

In this paper, we continue our analyses of the Great Observatories Origins Deep Survey (GOODS). GOODS aims to bring together the most powerful space and ground-based facilities to study the high-redshift universe across a wide range of wavelengths. We focus on

the southern GOODS field which has the greatest amount of multi-wavelength data essential for reliable stellar masses. The GOODS-S survey area covers a total of 160 arcmin^2 and is centered on the *Chandra* Deep Field South (CDF-S; Giacconi et al. 2002).

2.1. ACS Imaging

Deep optical imaging of GOODS-S has been obtained with the Advanced Camera for Surveys (ACS, Ford et al. 2003) instrument onboard *HST* as part of a Treasury Program (Giavalisco et al. 2004a). The Wide Field Camera on ACS has a field of $202 \times 202 \text{ arcsec}^2$ and a pixel scale of $0''.05$. The GOODS-South field was observed in the F435W (*B*-band), F606W (*v*-band), F775W (SDSS-*i'*) and F850LP (SDSS-*z'*) broad-band filters for 3, 2.5, 2.5 and 5 orbits, respectively over 16 pointings.

Here we present an analysis of $z \simeq 5$ galaxies making use of the publicly-available version-1.0 data-release of the ACS GOODS data¹. The reduced data have been ‘drizzled’ onto a large grid made up of 18 sections with a pixel scale of $0''.03$. Each section comprises an image of 8192×8192 pixels in size.

2.2. Ground-Based Near-infrared Imaging

Deep near-infrared observations of most of the GOODS-S field were obtained with the ISAAC camera on the Very Large Telescope (VLT) at the ESO Paranal Observatory as part of the ESO Large Programme: LP168.A-0485(A) (PI: C. Cesarsky). The publically available version-1.5 data release includes 24 fully reduced ISAAC/VLT pointings in the *J* and *K_s*-bands², covering $\approx 160 \text{ arcmin}^2$. Additional details of the observations are to be presented in Vandame et al. (2006, *in prep*). The VLT images have a pixel scale of $0''.15$, a factor of five times larger than the drizzled ACS pixels. The median exposure times are 11.3 ksec in *J*, and 17.9 ksec in *K_s*.

¹available from <ftp://archive.stsci.edu/pub/hlsp/goods/>

²available from <http://www.eso.org/science/goods/releases/20050930/>

2.3. Spectroscopy

We also use publicly-available spectroscopy from the GOODS team to identify confirmed $z \approx 5$ galaxies for further study. Multi-object spectroscopy was performed on the GOODS-S field with the FORS2 instrument mounted at the Kueyen Unit Telescope of the VLT at ESO’s Cerro Paranal Observatory as part of the ESO/GOODS Large Program LP170.A-0788 (PI Ciesarsky). Details of the survey are presented in Vanzella et al. (2002, 2005). The primary selection criteria for placing objects on the slitmask was $(i'_{775W} - z'_{850LP}) > 0.6$ and $z'_{850LP} < 25.0$; objects with $0.45 < (i'_{775W} - z'_{850LP}) < 0.6$ were placed on the slitmask with lower priority. We make use of the VLT/FORS2 spectroscopic catalogs from the version-2.0 release which provide 725 unique redshift assignments with quality flags A, B, or C (where A=solid redshift, B=likely redshift, C=potential redshift).

2.4. *Spitzer* Imaging

Spitzer images of GOODS-S were obtained with the Infrared Array Camera (IRAC) and Multiband Imaging Photometry for *Spitzer* (MIPS) cameras on the *Spitzer* Space Telescope as part of the “Super Deep” Legacy programme (PID 169, Dickinson et al. *in prep*, Chary et al., *in prep*). The IRAC camera comprises four channels, each with a 256^2 InSb array imaging a $5.2' \times 5.2'$ field with a pixel size of $\approx 1''.22$. Images were taken through four broad-band infrared filters, with central wavelengths at approximately $\lambda_{\text{cent}} = 3.6 \mu\text{m}$, $4.5 \mu\text{m}$, $5.6 \mu\text{m}$ and $8.0 \mu\text{m}$ (channels 1–4), and widths of $\Delta\lambda_{\text{FWHM}} = 0.68, 0.87, 1.25, 2.53 \mu\text{m}$ respectively. The total exposure time in each channel is ≈ 86 ksec, depending on location. The data were taken in two epochs, with the telescope roll angle differing by 180° . In the first epoch, each filter covered a $10.0' \times 10.0'$ area in GOODS-S; however, the area covered by channels 1 and 3 ($3.6 \mu\text{m}$ and $5.6 \mu\text{m}$) was offset by 6.7 arcminutes from that covered by channels 2 and 4 ($4.5 \mu\text{m}$ and $8.0 \mu\text{m}$). Hence, only a portion of the GOODS-S field was observed in all 4 filters after the first epoch of observations. In the second epoch, the area covered by channels 1 and 3 in the first epoch was observed with channels 2 and 4 and vice versa. A central overlap region appeared in both epochs, and this deeper area intentionally contains the Hubble Ultra Deep Field (HUDF, Beckwith et al. 2003; Bunker et al. 2004).

We analyze the publicly available *Spitzer* mosaics from the first and second epochs of the observations of GOODS-S³. The data reduction pipeline employs a ‘multidrizzle’ technique similar to that used successfully on *HST*/ACS GOODS data. This provides combined images

³available from <http://data.spitzer.caltech.edu/popular/goods>

with a pixel scale of $0''.6$. The magnitudes listed in this paper are determined from this ‘drizzled’ data. We use the updated “Super Deep” epoch 1 images from the third data release (DR3) and the Super Deep epoch 2 images from the second data release (DR2).

3. Photometric Samples

The photometry we compute in this section will be used for two independent samples of $z \simeq 5$ objects: a small sample of spectroscopically confirmed galaxies and a larger sample of photometrically selected galaxies. The spectroscopic sample will provide a robust lower limit to the $z \simeq 5$ stellar mass density whereas the photometric sample will provide a more representative estimate of the integrated mass density. To obtain stellar masses of individual galaxies, we must have accurate photometry for both samples as well as photometric redshifts for the photometric sample. The reliability of the photometric redshifts is especially crucial since contamination by low-redshift interlopers could seriously skew our estimates of the total mass.

We obtain photometric redshifts from the GOODS MUSIC photometric catalog of GOODS-S (Grazian et al. 2006). This catalog uses 13-band SEDs from *HST* /ACS and *Spitzer*/IRAC photometry along with ground-based U , J , & K_S to derive photometric redshifts. Before adopting the GOODS MUSIC photometric redshifts, we verify the accuracy of the photometry in the GOODS MUSIC catalog (discussed below) and test the reliability of their photometric redshifts which we discuss in §4.1.

ACS photometry was obtained from the GOODS team r1.1 catalog ⁴. The photometric zeropoints adopted in the catalog on the AB magnitude system are 25.653, 26.493, 25.641, and 24.843 for the B_{435W} -band, v_{606W} -band, i'_{775W} band, and z'_{850LP} -band, respectively. We have corrected for the small amount of foreground Galactic extinction using the *COBE*/DIRBE & *IRAS*/ISSA dust maps of Schlegel et al. (1998); for the GOODS-S field, selective extinction is given by $E(B - V) = 0.008$ mag. Magnitudes are measured in $0''.50$ -diameter apertures. Total magnitudes are derived from the aperture magnitudes by correcting for the small amount of light falling outside the aperture: 0.14, 0.15, and 0.20 mag in the v_{606W} , i'_{775W} , and z'_{850LP} -bands, respectively (Sirrianni et al. 2005). We note that GOODS website implies that the SExtractor parameter PHOT_APERTURES measures the *radius* of the photometric aperture, when it in fact measures the *diameter*. The correct interpretation has been applied to our dataset.

⁴available from <http://archive.stsci.edu/prepds/goods>

Near-infrared photometry was performed with $1''$ -diameter apertures using the ground-based near-infrared ISAAC images. The center of the photometric aperture was taken from the centroid of the GOODSr1.1 catalog. The seeing varied across the ISAAC field as different tiles were taken over many nights, so we determined separate aperture corrections from unresolved sources for each tile. For the J - and K_s -band images the seeing is typically good ($\text{FWHM} = 0''.4 - 0''.5$), and the aperture corrections are $\approx 0.3 - 0.5$ mag, determined from bright but unsaturated isolated stars measured in $6''$ -diameter apertures. The 3σ limiting AB-magnitudes in a $1''$ -diameter aperture are $J \approx 26.4$ and $K_s \approx 25.7$, although these vary over the field because of different exposure times and seeing conditions.

The details of the photometric analysis of the Spitzer images used in this paper are nearly identical to those presented in Eyles et al. (2005). In order to maximize the signal-to-noise ratio (S/N) and minimize possible confusion with other foreground objects, we used a photometric aperture of diameter $\approx 1.5 \times \text{FWHM}$ for the IRAC images, appropriate for unresolved objects (our compact sources are essentially unresolved at IRAC resolution, see e.g. Bremer et al. 2004). The aperture diameters were 4, 4, 5 & 6 ‘drizzled’ pixels for the 4 channels (3.6, 4.5, 5.6 & $8.0 \mu\text{m}$), corresponding to $2''.4$, $2''.4$, $3''.0$, & $3''.7$. We used the IRAF `digiphot.phot` package to measure the enclosed flux at the coordinates determined by the ACS GOODS-r1.1 catalogs, taking the residual background from an annulus between $12''$ and $24''$ radius. We applied aperture corrections to compensate for the flux falling outside the aperture: these were ≈ 0.7 mag for the IRAC data, as determined from bright but unsaturated point sources in the images using large apertures.

The noise for each of the four channels was checked in two different ways. First, we derived an estimate based on a Poisson model using the detector gain, number of frames combined, and the background counts (adding back the zodiacal background estimate subtracted by the pipeline but recorded in the header). Secondly, we measured the standard deviation in background counts of the images. As the mosaicking process introduces correlations between pixels, we also made noise estimates using the individual pipeline basic calibrated data (BCD) images and assuming it decreased as the square root of the number of frames. These estimates lead to 3σ limiting AB magnitudes of 26.5 and 26.1 using $2''.4$ -diameter apertures in channels 1 and 2, respectively, and 23.8 and 23.5 in $3''.0$ and $3''.7$ -diameter apertures in channels 3 and 4, respectively. There will be additional background fluctuations caused by faint galaxies (i.e. confusion noise), which will increase the noise. Both methods produce consistent estimates.

The low spatial resolution of *Spitzer* results in frequent blending between nearby sources, making accurate photometry of individual objects difficult. We took great effort to ensure that objects in our sample were not contaminated by neighboring bright foreground sources.

We approach the IRAC contamination in slightly different ways for the different subsamples of $z \simeq 5$ objects. Details are provided in §4.

We find that our photometry is consistent with that in the GOODS MUSIC catalog. The standard deviation between our photometry and the GOODS MUSIC photometry is 0.13 mags, 0.03 mags, 0.13 mags for the z' , J, and K band. This increases to 0.36 mags for the 3.6 micron IRAC photometry.

4. Selection of $z \simeq 5$ Galaxies

4.1. The Photometric Sample

We make use of the extensive database of photometric redshifts in the publicly-available GOODS-MUSIC catalog (Grazian et al. 2006) to construct a sample of $z \simeq 5$ candidates. Details of the procedure used to compute the photometric redshifts are discussed in Grazian et al. (2006). As described below, we based our photometric selection on the GOODS-MUSIC catalog rather than upon a more traditional v -band dropout technique (Bremer et al. 2004; Giavalisco et al. 2004a; Yan et al. 2005) on account of the improved performance in various tests. The principle difference is that the former method is based on fitting the entire SED.

First, we consider the fidelity of the GOODS-MUSIC selection of $z \simeq 5$ galaxies with respect to the VLT spectroscopic results of Vanzella et al. (2002, 2005). 21 galaxies within our $z \simeq 5$ spectroscopic sample (see next section) have photometric redshifts in the GOODS-MUSIC catalog. 18 of these ($>85\%$) have photometric redshifts in the $4.4 < z < 5.6$ range with an average absolute scatter of $< |z_{\text{spec}} - z_{\text{phot}}| > 0.07$. Two of the three objects for which the photometric redshifts fail completely (e.g photometric redshifts of $z \simeq 1 - 2$) have spectroscopic redshift quality grades of C: here it is possible that the photometric redshifts are actually correct. This test suggests the SED-fitting process is reasonably accurate.

A further verification of the reliability of the photometric catalog concerns the implied rest-frame colors. Adopting a magnitude limit of $z'_{850LP} < 26.5$ (the 50% completeness limit for unresolved sources in GOODS Giavalisco et al. 2004a), we find 214 objects with photometric redshifts between $4.4 < z < 5.6$. Their rest-frame UV colors are in uniformly good agreement with those expected from the locus of star-forming galaxies at $z \simeq 5$ (Figure 1).

We find that only 42% of the objects in our photometric catalog would have been selected in the traditional Giavalisco et al. (2004a) v -drop method. Examining the redshift tracks, it is clear that the v -drop method misses a significant fraction of $z = 4.5 - 5.5$

star-forming galaxies (Figure 1). This region of color-color space is not included in the traditional v -drop method to minimize the inclusion of low redshift contaminating galaxies. The GOODS-MUSIC photo- z sample (along with the criteria we impose below) represents an improvement to the traditional v -drop selection criteria as it takes the entire SED into consideration in assessing an object’s redshift.

While the GOODS-MUSIC photometric redshifts appear to be an excellent predictor of the true redshift, we remain vigilant to the possibility of a few catastrophic failures. The point is critical as the presence of any residual low redshift or stellar objects that are very bright at *Spitzer* wavelengths could lead to a significant overestimate of the stellar mass density. Recognizing there is a danger of removing true $z \simeq 5$ sources, we conclude it is better to err on the conservative side.

Because of their red colors, low-mass stars are a common contaminant of photometrically-located high redshift galaxy samples. Bright stars can be removed from high- z galaxy samples by selecting unresolved objects in the HST/ACS images. However, this technique begins to fail at fainter magnitudes as extragalactic objects may appear unresolved if observed at low S/N. Alternatively, stellar contaminants can be selected from our sample on the basis of their optical through near-infrared. We fit the SEDs of all objects in the photometric catalog with M, L, and T dwarf stellar templates (Leggett et al. 2002; West et al. 2005; Kraus et al. 2006). We construct a list of stellar contaminants by examining each object well-fit with stellar colors, only including sources without extended emission. Our final list consists of 11 stars (5% of the total sample) with $z'_{850LP} = 24.3 - 26.5$, each of which we remove from our photo- z sample.

Low-redshift galaxies with intrinsically red colors arising from dust extinction or an old stellar population commonly contaminate traditional dropout samples because their ($v_{606W} - i'_{775W}$) colors are similar to those of $z \simeq 5$ star-forming objects. By considering the shape of the entire SED, low- z interlopers can often be identified and removed from high-redshift dropout samples. Since the GOODS-MUSIC photometric redshifts are computed using the entire SED, we expect the contamination rate from low- z galaxies to be low. Nevertheless, we believe it is important to explore the possibility that low-redshift galaxies may remain in the GOODS-MUSIC sample and examine the effects that possible contaminants may have on our final results.

A simple way to estimate the contamination rate from low- z galaxies is to measure the rest-frame UV–optical colors of each of the objects in our sample. Unextincted star-forming objects at $z \simeq 5$ typically have spectra that are roughly flat in f_ν (as a function of wavelength) between the Lyman break and rest-frame $\simeq 4000$ Å. In contrast, the colors of low-redshift contaminants are red in all filters. To quantify the expected difference in

rest-frame UV–optical colors between $z \simeq 5$ sources and possible low- z contaminants, we examined a set of Bruzual & Charlot (2003) population synthesis models. Elliptical galaxies at $z \simeq 1\text{--}2$ with ages > 2 Gyr have $(z'_{850LP} - J)$ colors that vary between 1.4 - 1.6; whereas young ($\simeq 100$ Myr) star-forming galaxies at $z \simeq 5$ with $E(B-V)=0.0\text{--}0.2$ have $(z'_{850LP} - J)$ colors ranging between -0.1 and -0.3 . Accordingly, to test the low- z contamination rate, we adopt a $(z'_{850LP} - J) > 1.0$ threshold⁵ above which we consider galaxies to be possible low- z interlopers. Seven objects in our photo- z sample satisfy this color criterion. Six of the seven objects are relatively faint in the IRAC filters, and thus will hardly contribute to the total stellar mass of the sample. One of the objects (23_18055), however, is very bright in the near and mid-infrared ($m_{3.6\mu m}=21.1$); if at $z \simeq 5$, its best-fit stellar mass would be $2 \times 10^{12} M_{\odot}$. Given that no objects are identified at $z > 4$ with stellar masses above $3 \times 10^{11} M_{\odot}$ in the 0.8 sq deg UKIDSS survey (Dunlop et al. 2006), we conclude that it is much more realistic to adopt a low- z interpretation for this object. So as not to bias our total mass estimates we remove the seven objects with $(z'_{850LP} - J) > 1.0$ from our photo- z sample, leaving 196 objects.

The final photometric sample is that for which the *Spitzer* IRAC images reveal a clear, unconfused, detection. Reliable stellar masses cannot otherwise be determined. We examined the *Spitzer* images of each of the 196 $z \simeq 5$ candidates, classifying them as either (1) isolated and detected, (2) undetected, (3) confused or (4) hopelessly confused. In the subsequent analysis, we consider only those objects that are detected and isolated. Of the 196 candidates, 72 are sufficiently uncontaminated to allow reliable estimates of the stellar mass.

Table 1 lists the measured optical through infrared AB magnitudes (corrected to approximate total magnitudes through an aperture correction), colors, and photometric redshifts for the remaining 72 $z \simeq 5$ objects.

4.2. The Spectroscopic Sample

The FORS2/VLT spectroscopic survey of the GOODS-S field identified 30 unique galaxies in the $4.4 < z < 5.6$ redshift range. The quality flags associated with the redshift assignments range from A (solid) to C (potential). As with the photometric sample, we adopt a magnitude limit of $z'_{850LP} < 26.5$; this requirement excises one object (35_11820) from the sample. Given the possibility of uncertainties in the spectroscopic identification of those sources with C-grade redshifts, we examined their rest-frame ultraviolet colors ($v_{606W} - i'_{775W}$) vs. $(i'_{775W} - z'_{850LP})$ as an additional criterion for selection (Figure 2).

⁵The precise value of this color discriminant is not critical in defining the final sample

Of the 29 remaining FORS2 galaxies with spectroscopic redshifts of $z \simeq 5$, only 17 would be selected as v -drops using the Giavalisco et al. (2004a) selection criteria. An additional 8 of the spectroscopically-confirmed $z \simeq 5$ galaxies fall very near the v -drop selection window in the $(v_{606W} - i'_{775W})$ vs. $(i'_{775W} - z'_{850LP})$ color-color plot. As their colors are consistent with the Bruzual & Charlot redshift tracks (plotted in Figure 2) we include them in this sample. Three objects are apparently undetected in the *ACS* images of GOODS-S. Without the availability of rest-frame UV colors, we cannot confirm that the objects are truly located $z \simeq 5$ via the presence of the Lyman break; we presume these were serendipitous detections and exclude them from the final spectroscopic sample. The final object (22_15184) is formally a B-dropout; its relatively blue $(v_{606W} - i'_{775W})$ color is inconsistent with that expected from a v -drop. At the object’s purported redshift ($z = 5.08$) $\text{Ly}\alpha$ falls in the i' -band, making the intrinsic $(v_{606W} - i'_{775W})$ *bluer* than what is measured. Given the peculiar colors, we exclude it from the spectroscopic catalog.

As before, we examined the *Spitzer* images of each of the 25 spectroscopically-confirmed galaxies for detections and the degree of confusion. These classifications are shown in Table 2. Five objects were isolated and detected in the *Spitzer* images, four sources were hopelessly confused, and the remaining 16 objects were marginally confused. For the 16 partially confused galaxies, we attempted to subtract the contribution from contaminating sources using the ‘GALFIT’ software package (Peng et al. 2002); this was deemed worthy given the need to maximize the information from the limited spectroscopic data.

GALFIT constructs a two-dimensional model of the data according to specified input parameters (e.g., magnitude, position, axis ratio, effective radius), performs a convolution with the instrument point spread function (PSF), and fits the result to the data through an iterative χ^2 minimization process. We determined the PSF for each epoch and channel of the ‘drizzled’ *Spitzer* images by stacking 4 bright but isolated stars. For each galaxy we assumed a generalized Sérsic surface brightness profile, where $\log I \propto r^{1/n}$, and fit for the shape and index n .

An automated script was developed to run GALFIT three times per source on a $12 \times 12 \text{ arcsec}^2$ region surrounding the contaminated object for the IRAC images. In the first iteration, we held all source parameters fixed in the fitting process except the source magnitude, which was estimated from the SExtractor source detection software version-2.2.1 (Bertin & Arnouts 1996). All other input source parameters (e.g. position, axis ratio, position angle, effective radius, Sérsic parameter) were estimated from a fit to the VLT K_s -band image. The higher spatial resolution of the K_s -band allows better deblending and more accurate centroids to be derived for confusing objects in the IRAC images. In the second GALFIT iteration, we again determined input parameters using our fit to the K_s -band im-

age, but this time we allowed all parameters to vary. In the final iteration, we obtained the initial parameters by applying SExtractor to the IRAC channel 1 ($3.6\mu\text{m}$) image and allowing all parameters to vary. For each source, we selected the most successful of the three GALFIT runs, on the basis of visual inspection of the residual image and the χ^2 value for the fit. Those sources (7 out of 16) for which GALFIT failed to satisfactorily subtract contaminating emission were removed from the sample (see Table 2). The photometry of the remaining 14 galaxies are described in Table 3.

5. Stellar Mass Determination

Although we have removed many sources from the original spectroscopic and photometric samples, it is worth reminding that the degree of confusion in the IRAC images should, on average, be completely independent of the stellar mass of the $z \simeq 5$ galaxy. Confusion in the IRAC images will normally arise from the overlapping isophotes of unrelated sources. Thus, if sources are believed to be at $z \simeq 5$ on the basis of a spectroscopic redshift or the ACS and K -band photometric SED, we can rescue a reasonable estimate of their contribution to the stellar mass density by scaling that determined for the unconfused sample using the relative numbers.

5.1. Masses for the Spectroscopic Sample

For those galaxies with confirmed spectroscopic redshifts, we estimate stellar masses by fitting population synthesis models to the observed SEDs. Applying this technique to galaxies for which the redshift is unknown may lead to significant uncertainty in the derived properties (Bundy et al. 2005; Shapley et al. 2005), hence for the photometrically-selected sample, we infer stellar mass by applying the median mass-to-light ratio derived from the spectroscopic sample.

We proceed as Eyles et al. (2005) by fitting the latest Bruzual & Charlot (2003) stellar population synthesis models to the observed SEDs. We use the Padova evolutionary tracks preferred by Bruzual & Charlot (2003). The models utilise 221 age steps from 10^5 to 2×10^{10} yr, approximately logarithmically spaced. For each source, we do not include age steps in excess of the age of the universe at $z \simeq 5$ ($\simeq 1.2$ Gyr). Models with Salpeter (1955) initial mass functions (IMF) were selected; although we also considered the effect of adopting a Chabrier (2003) IMF. There are 6900 wavelength steps, with high resolution (FWHM 3\AA) and 1\AA pixels evenly-spaced over the wavelength range of 3300\AA to 9500\AA (unevenly spaced

outside this range). From the full range of metallicities offered by the code, we considered both solar and $0.25 Z_{\odot}$ models. From several star formation histories available, a single stellar population (SSP – an instantaneous burst), a constant star formation rate (SFR), and exponentially decaying (τ) SFR models with e-folding decay timescales $\tau=10, 30, 50, 70, 100, 200, 300, 500, 1000$ Myr were used.

For each of the galaxies in our sample, the filters were corrected to their rest-frame wavelengths by the appropriate redshift factor. The measured flux was folded through the filter transmission profiles, and the best-fit age model was computed by minimizing the reduced χ^2 , using the measured errors on the magnitudes. The number of degrees of freedom is the number of independent data points (magnitudes in different wavebands) minus the number of parameters that we are fitting. The Bruzual & Charlot spectra are normalized to an initial mass of $1 M_{\odot}$ for the instantaneous burst (SSP) model, and an SFR of $1 M_{\odot} \text{ yr}^{-1}$ for the continuous star formation model. The fitting routine returned the normalisation for the model which was the best-fit to the broad band photometry (i.e., minimized the reduced χ^2). This normalization was then used to calculate the corresponding best-fit total mass using the luminosity distance for the redshift of each source. When considering models other than an SSP (instantaneous burst), it was necessary to correct the total ‘mass’ values output by the fitting routine. For a constant SFR model, each of these masses needed to be multiplied by the corresponding best-fit age, since the B&C template normalization has the mass grow by $1 M_{\odot} \text{ yr}^{-1}$. For the exponential decay models, the returned mass values were corrected by dividing by $(1 - e^{-t/\tau})$, accounting for the decay timescale and the normalization of the B&C models (where $M \rightarrow 1 M_{\odot}$ as $t \rightarrow \infty$). The fits to the B&C models returned the ‘total mass’ which is the sum of the mass currently in stars, in stellar remnants, and in gas returned to the interstellar medium by evolved stars. For each best-fit model, we subsequently calculate the mass currently in stars for every galaxy, again using information from the B&C population synthesis code; we use this stellar mass in all future analysis.

Although some of our data points (particularly from the *HST*/ACS imaging) have $S/N > 10$, we set the minimum magnitude error to be $\Delta(\text{mag}) = 0.1$ to account for calibration uncertainties. Furthermore, we do not include data with photometric error above 0.72 mags (1.5σ).

The presence of a strong spectral line in one of the broadband filters could significantly skew the SED fitting. Seven of the 15 galaxies in our spectroscopic sample show powerful $\text{Ly}\alpha$ emission. Using the FORS2 spectra, we compute and subtract the $\text{Ly}\alpha$ contribution to the broadband flux; corrections range from 0.01 – 0.1 mags for most sources. $\text{H}\alpha$ contamination could also be a significant issue - Chary et al. (2005) claim to find an excess due to $\text{H}\alpha$ in a $z=6.5$ galaxy (in the $4.5\mu\text{m}$ band at that redshift). The sources in our sample are likely to

have $H\alpha$ emission lines as well, which at $z \simeq 5$ fall in either the $3.6 \mu\text{m}$ or $4.5 \mu\text{m}$ IRAC filter. Indeed many of the SED fits discussed below show an excess at $3.6 \mu\text{m}$. Without a direct measure of the $H\alpha$ line strengths, we cannot robustly remove the line contamination. We estimate that, for most sources, $H\alpha$ contributes $\simeq 10\text{-}20\%$ of the measured broadband flux by converting the inferred rest-frame UV star formation rate to an H-alpha luminosity via empirically-derived relations from Kennicutt (1998) assuming $\langle SFR_{H\alpha}/SFR_{UV} \rangle = 1.5\text{-}3$ due to dust extinction in agreement with observations, e.g. Erb et al. (2003). To test the effects that $H\alpha$ contamination may have on our sources, we re-fit all the objects in the spectroscopic sample, omitting the flux information at $3.6 \mu\text{m}$ for objects with $z < 5.2$ and at $4.5 \mu\text{m}$ for objects with $z > 5.2$. We find that this does not significantly change the total stellar mass found in our spectroscopic sample.

The degeneracies associated with the derived best-fit parameters from SED fitting are well known (Shapley et al. 2001; Papovich et al. 2001; Shapley et al. 2005). The uncertainties primarily stem from a poor knowledge of the form of the star formation history, since the best fit age, dust extinction and star formation rate rely on this (Shapley et al. 2005). In most cases, the data do not put strong constraints on the form of the star formation history; hence each fitted parameter typically has a range of values that produce acceptable fits.

The inferred properties also rely on knowledge of the stellar initial mass function (IMF). There is little observational information constraining the IMF at high redshift. The spectrum of the $z=2.7$ gravitationally-lensed LBG cB58 appears to be inconsistent with IMFs that have steep high-mass slopes or are truncated at high stellar masses (Pettini et al. 2000). Whether this is typical among LBGs is unclear. Papovich et al. (2001) studied the effects that varying the IMF have on the best-fit parameters. Models with IMFs containing steep high-mass slopes (e.g. Scalo, Miller-Scalo) have redder integrated spectra and hence younger derived ages and lower extinction. As with Eyles et al. (2005), we find good agreement between the properties inferred using a Salpeter IMF and a Chabrier IMF: the best-fit ages are nearly the same and the stellar masses are typically 30% lower when the Chabrier IMF is used. Here all masses are quoted for the Salpeter IMF in order to maintain consistency with previous estimates of stellar mass and star formation rates.

In Figure 4, we display the best-fit SEDs for each of the galaxies in our spectroscopic sample. The best-fitting model parameters are presented in Table 4. The best fitting stellar masses of the galaxies range between $3 \times 10^8 M_{\odot}$ and $2 \times 10^{11} M_{\odot}$. Derived ages span three orders of magnitude, from 1 Myr to 1.1 Gyr, the age of the Universe at $z \simeq 5$. Interestingly, three of our sources have stellar masses in excess of $10^{11} M_{\odot}$, values approaching the high stellar mass for the UDF source located by Mobasher et al (2005). Our results provides support for at least the presence of such galaxies even if their abundance remains uncertain.

Moreover, some of the less massive sources can only be fit with remarkably young ages (< 20 Myr) reminiscent of the lensed star forming source located by Ellis et al. (2001).

The total stellar mass of the subsample of spectroscopic galaxies is $5 \times 10^{11} M_{\odot}$. Clearly this estimate is an *unrealistic* lower limit to the total stellar mass since there are nearly twice as many objects known to be at $z \simeq 5$ that certainly have stellar mass.

Uncertainties on this mass arise from two main sources. First, the photometric error for each data-point in the SED translates into an uncertainty in the inferred stellar mass. Second, there is a range in acceptable masses that result from varying the age, extinction, and star formation history. With regard to the latter, we follow the approach outlined in Eyles et al. (2005) where confidence intervals were explored for two sources. We present mass-age confidence intervals for two sources representative of our sample (Figure 5). Uncertainties in the inferred stellar mass of individual objects in Table 4 range between 30% and 50%. Objects detected at low signal to noise generally have larger uncertainties. Given the range of uncertainties, it seems reasonable to transfer a 50% uncertainty to all of our combined masses.

The FORS2 selection of galaxies was not geared specifically towards constructing a $z \simeq 5$ sample; hence it is important to examine how the properties of spectroscopically-confirmed galaxies compares to the photometrically-selected sample. The median rest-frame UV color of the spectroscopic sample, $\langle i'_{775W} - z'_{850LP} \rangle = 0.17$, is very similar to the photometrically-selected sample $\langle i'_{775W} - z'_{850LP} \rangle = 0.21$. The key parameter for determining the stellar mass is the flux in the IRAC filters. The histogram of IRAC $3.6 \mu\text{m}$ fluxes for the spectroscopic and photometric samples is given in Figure 3. The spectroscopic sample does contain a larger fraction of Spitzer-bright (e.g. $m_{3.6\mu\text{m}} < 23$) objects, but this is reasonable if the overall rest-frame mass/light distribution is fairly similar across the population.

5.2. Masses for the Photometric Sample

To estimate stellar masses for the photometric sample we compute the best-fitting rest-frame V -band mass to light ratio of each galaxy that is unconfused in the IRAC images and multiply by the luminosity derived from the IRAC flux.

The best-fitting M/L_V is determined for each galaxy from its $z'_{850LP} - m_{3.6\mu\text{m}}$ color (corresponding to the ratio of rest-frame UV and optical fluxes). If we assume the typical galaxy in rest-frame UV selected samples at $z \simeq 5-6$ has little dust as seems reasonable (see Table 4 and Eyles et al. 2006), then the $z'_{850LP} - m_{3.6\mu\text{m}}$ color is correlated with the age of the galaxy and hence, for a given IMF and star formation history, its M/L_V ratio.

This is done for a given galaxy in the sample by first computing $z'_{850LP} - m_{3.6\mu m}$ colors for Bruzual-Charlot models (redshifted to the galaxy’s photometric redshift) with ages ranging between 0 and 1.2 Gyr (roughly the lookback time at the redshift of the galaxy). We then find the model that produces the $z'_{850LP} - m_{3.6\mu m}$ color closest to that observed for a given galaxy. This model is taken to have the “best-fit” age and M/L_V ratio for this particular galaxy. At $z \simeq 5$, the $3.6\mu m$ IRAC filter covers the rest-frame V-band; hence, we convert the $3.6\mu m$ flux to a luminosity (assuming $z = z_{phot}$) and multiply it by the best-fitting M/L_V to compute the stellar mass. For each galaxy, best-fitting stellar masses are computed for the same range of single-component star formation histories used to fit the spectroscopic sample. The stellar mass we assign to each galaxy is taken from the star formation history that produces the best-fitting $z'_{850LP} - m_{3.6\mu m}$ colors. We obtain an estimate of the systematic uncertainty in the mass by considering the range inferred from the different star formation histories and ages that provide a good fit (e.g. $\Delta\chi^2 = \chi^2 - \chi^2_{min} < 1$) to the observed $z'_{850LP} - m_{3.6\mu m}$ color.

We note that the observed $3.6\mu m$ luminosity is not equivalent to a rest-frame V-band luminosity for all redshifts. The $3.6\mu m$ band shifts between rest-frame 5500-6700 Å for $z = 4.4$ -5.5. To test the systematic offsets introduced by relying on M/L_V to derive masses, we compare the mass of the spectroscopic sample derived in the manner described above to the mass from SED fitting. We find the median offset between the two methods is 40%.

The total stellar mass extracted from the 72 $z \simeq 5$ sources that are uncontaminated in the Spitzer images is $5 - 9 \times 10^{11} M_\odot$ with a best-fit value of $7 \times 10^{11} M_\odot$. The median stellar mass in the sample is $6 \times 10^9 M_\odot$. If we make the reasonable assumption that the distribution of stellar masses is independent of IRAC contamination, we can estimate the stellar mass in IRAC contaminated galaxies by multiplying the stellar mass derived from the uncontaminated $z \simeq 5$ galaxies by the ratio of the total number of $z \simeq 5$ sources to the number of uncontaminated $z \simeq 5$ sources. Following this reasoning, the total stellar mass for the photometric sample becomes $2 \times 10^{12} M_\odot$. Taking the full range of single-component star formation histories into consideration, this total stellar mass could lie between 2 and $3 \times 10^{12} M_\odot$.

5.3. Comoving Mass Densities

To derive the comoving stellar mass densities from the above totals, we need to estimate the redshift-dependent selection function in the 160 arcmin² GOODS-S field between $4.4 < z < 5.6$. Although the total possible comoving volume is $5.6 \times 10^5 \text{ Mpc}^3$, the effective volume is less than this value due to sample incompleteness arising as a result of objects being

scattered faintward of the magnitude limit or out of the color-selection window.

In order to account for these luminosity and redshift biases, we compute an effective survey volume following the approach of Steidel et al. (1999) using

$$V_{\text{eff}}(m) = \int dz p(m, z) \frac{dV}{dz} \quad (1)$$

where $p(m, z)$ is the probability of detecting a galaxy at redshift z and apparent z' magnitude m , and $dz \frac{dV}{dz}$ is the comoving volume per unit solid angle in a slice dz at redshift $z = 4.4\text{--}5.6$.

We compute the probability function $p(m, z)$ by putting thousands of fake galaxies into the GOODS images and recreating a photometric catalog for the new image using identical selection parameters used in generating the GOODSv1.1 catalogs. The apparent magnitudes of the fake galaxies span $z'_{850LP} = 22\text{--}27$ in steps of $\Delta m = 0.5$ and redshifts ranging between $z = 4$ and $z = 6$ in steps of $\Delta z = 0.1$. The sizes of the fake galaxies are consistent with distribution of half-light radii derived for $z \simeq 5$ galaxies in Ferguson et al. (2004). The colors of the fake galaxies depend on the galaxy redshift and SED. We adopt the SED of a Bruzual-Charlot model with constant star formation history, an age of 100 Myr, and no dust as the intrinsic rest-frame SED of the fake galaxies. Allowing for a selective extinction of $E(B-V) = 0.1$ in the fake galaxies' SEDs decreases the effective volume by roughly 5%, which would not significantly change our final mass density estimates. The colors are then determined for galaxies at each redshift in a manner similar to that which we described in §5.1. The probability function, $p(m, z)$ is then given by the fraction of fake galaxies with apparent magnitude, m , and redshift, z , that are brighter than the magnitude limit and satisfy the dropout color selection criteria. Since our selection is based on photometric redshifts, we adopt color-criteria that are appropriate for our photometric sample ($v_{606W} - i'_{775W} > 0.9$ and $i'_{775W} - z'_{850LP} > 1.3$).

The effective volume probed is $5.2 \times 10^5 \text{ Mpc}^3$ at $z'_{850LP} = 23$ and $z = 5$ where we are nearly 100% complete and falls to $1.2 \times 10^5 \text{ Mpc}^3$ at $z'_{850LP} = 26.5$. The stellar mass density inferred from our $z \simeq 5$ candidates is thus $5\text{--}8 \times 10^6 \text{ M}_\odot \text{ Mpc}^{-3}$, with a best-fit value of $6 \times 10^6 \text{ M}_\odot \text{ Mpc}^{-3}$. The robust lower limit from our spectroscopic sample is $1 \times 10^6 \text{ M}_\odot \text{ Mpc}^{-3}$.

Our inferred stellar mass density is most likely an underestimate of the total value at $z \simeq 5$ for several reasons. Foremost, the survey is only sensitive to the most luminous and perhaps most massive galaxies since we only included objects with significance above 3σ at $3.6\mu\text{m}$.

Second, an additional reservoir of stellar mass may be contained in objects that are not currently forming stars and hence are very faint in the rest-frame ultraviolet. At $z \simeq 3$, LBGs contribute only 17% of the stellar mass density in the most massive sources

(van Dokkum et al. 2006); the remaining fraction is likely contained in objects that are not actively forming stars. Although this fraction of quiescent sources is probably much lower at earlier times, we conservatively estimate the total mass density could rise by a further factor of two.

In summary, therefore, we derive a firm lower limit to the stellar mass density at $z \simeq 5$ of $1 \times 10^6 \text{ M}_\odot \text{ Mpc}^{-3}$, a reasonable estimate of the total *observed* population of $5\text{--}8 \times 10^6 \text{ M}_\odot \text{ Mpc}^{-3}$ and cannot exclude undetected sources which would increase the total to $1 \times 10^7 \text{ M}_\odot \text{ Mpc}^{-3}$. Although the overall estimates span a factor of 2, we emphasize that the spectroscopic sample is clearly a significant underestimate of the observed population.

6. Implications for the Previous Star Formation History

In the foregoing we have attempted to put the first bounds on the stellar mass density at $z \simeq 5$, 1.2 Gyr after the Big Bang and about 800 Myr after $z \simeq 10$. We emphasize that there are considerable uncertainties in the various steps in our analysis. First, to derive stellar mass estimates, we had to cull our samples to those with reliable IRAC detections, later scaling on the assumption that they represent a fair subset of the spectroscopic and photometric populations. For our spectroscopic sample, our fitting procedure gives mass estimates that span a wide range depending on the assumed star formation history. Finally, we assumed a median visual mass/light ratio for the photometric sample derived from that for the spectroscopic sample.

Probably the dominant error in deriving the total mass density is not the numerical scaling factors, but rather the intrinsic uncertainty in estimating the masses of individual galaxies. Detailed work at lower redshift (Shapley et al. 2005; Bundy et al. 2005; Papovich et al. 2005) has shown that inferences of the stellar mass from SED fitting yield mass estimates that contain typical uncertainties of $\simeq 30\%$. The errors certainly increase slightly when considering objects at higher redshift; however, our error estimates (§5.1) suggest that the stellar mass estimates of objects in our spectroscopic sample are typically 50%, possibly more.

Notwithstanding the uncertainties, it is interesting to now consider the implications of our derived mass density. The star formation rate density (SFRD) of bright ($> 0.3 L_{z=3}^*$) star-forming galaxies at $z \simeq 5 - 10$ appears to decline continuously toward higher redshift (Bunker et al. 2004; Bouwens et al. 2004, 2005). However, current observations may be missing a substantial fraction of star formation either because it is enshrouded in dust, too faint to be detected with current facilities, or located at redshifts uncharted by current telescopes ($z > 10$). Comparing the comoving density of assembled stellar mass at $z \simeq 5$

with estimates derived from models of the previous star formation history enables us to test these possibilities, thereby providing constraints beyond direct reach of current facilities.

Taking data on the SFRD from the recent literature (Giavalisco et al. 2004a; Bouwens et al. 2004; Stanway 2004; Bouwens et al. 2005, 2006), we fit the redshift dependence with a simple functional form over $z \simeq 5 - 10$. In cases where the SFRD was not evaluated down to the adopted fiducial luminosity limit ($0.1L^*$ at $z=3$), we compute the additional contribution by integrating the luminosity function assuming the Schechter function parameters derived in each paper. Since the data at $z > 7$ do not allow for the robust derivation of the form of the luminosity function, we assume the shape of the luminosity function remains constant before $z \simeq 6$.

As Bouwens et al. (2006) discuss, at $z \simeq 6$ there is some disagreement in the value of the SFRD. The disagreement stems primarily from whether the shape of the luminosity function is evolving. Bouwens et al argue for a decrease in the characteristic luminosity and an increase in the faint end slope prior to $z \simeq 3$, so we adopt the redshift-dependent LF parameters derived in Bouwens et al. (2006) and Stanway (2005) and integrate accordingly. We find that the SFRD (integrated down to $0.1 L_{z=3}^*$) can be fit reasonably well by $\rho \propto (1+z)^{-3.3}$ between $z=5-10$ (Figure 6).

The stellar mass density obtained by integrating this function over time between $z \simeq 10$ and $z \simeq 5$ is lower than that derived from the photometric sample of $z \simeq 5$ objects in this paper (Figure 7). We note that the integral of the star formation rate density as a function of redshift overestimates the mass density. This is because we do not account for the mass that is returned to the interstellar medium in stellar winds and stellar deaths. This can be quantified using the Bruzual & Charlot (2003) software (we do this to compute stellar masses, see §5.1), but it is a complicated function of the average star formation history and age, which are not well-constrained. We find that this effect could *reduce* the stellar masses inferred from integrating the observed star formation rate densities by up to $\simeq 30\%$ (assuming a 1 Gyr instantaneous burst). Given the uncertainties, we do not adjust the curves in Figure 7 by this factor, but we note that this effect further enhances the discrepancy between the observed stellar mass density at $z \simeq 5$ and that which can be accounted for by previous star formation. Therefore, the observed stellar mass of the $z \simeq 5$ galaxies in GOODS-S either implies a significant amount of dust extinction or that not all star formation at $z > 5$ has been observed in current surveys.

To examine the amount of star-formation that may be hidden in low-luminosity systems, we integrate the luminosity functions to zero luminosity utilizing faint-end slopes of $\alpha = -1.73$ (as measured at $z \simeq 6$ in Bouwens et al. 2006) and $\alpha = -1.9$ (as suggested by Yan & Windhorst 2004) and integrate the luminosity function to zero luminosity.

Star formation is unlikely to occur at very low luminosities because of radiative feedback processes and (after reionization) a photoionized IGM which raises the cosmological Jeans mass. We nonetheless take this extreme approach to place an upper limit on the amount of unextincted star formation. Assuming no evolution in the shape of the LF between $z \simeq 5$ and $z \simeq 11$, this increases the predicted stellar mass at $z \simeq 5$ by an extra factor of 2.3 for faint end slopes of $\alpha = -1.73$; if we instead consider an extreme faint-end slope of $\alpha = -1.9$, the star formation rate density increases by a factor of 6.8. This gives a better account of the assembled mass and if correct has interesting consequences for higher redshift surveys probing to low luminosities Stark et al. (2007).

A significant amount of star formation may also be enshrouded by dust. However, recent observations have shown that the rest-frame UV slope of $z \simeq 6$ galaxies is actually somewhat *bluer* than that at $z \simeq 3$ suggesting that the mean dust extinction declines between $z \simeq 3$ -6 (Stanway et al. 2005; Yan et al. 2005; Bouwens et al. 2006). Taking the empirically derived fit relating the extinction at 1600 Å (A_{1600}) to the UV slope β , $A_{1600} = 4.43 + 1.99\beta$ (Meurer et al. 1999) yields an overall attenuation factor of $\times \simeq 1$ -1.5 at $z \simeq 6$ for two different estimates of the UV continuum slope at $z \simeq 6$ ($\beta = -2.2$ from Stanway et al. 2005 and $\beta = -2.0$ from Bouwens et al. 2006).

Hence, the expected extinction correction to the SFR density at $z \simeq 5 - 10$ could in principle account for the stellar mass contained in the photometric sample in this paper if the Bouwens et al. (2006) estimate of the UV continuum slope is correct. If there exists either a significant population of quiescent massive galaxies or low-mass galaxies below the 3σ $3.6 \mu\text{m}$ flux limit imposed on the data, a significant amount of low-luminosity star-forming galaxies would be required to assemble the stellar mass. Future studies will test this hypothesis.

7. Conclusions

We have argued that the assembled stellar mass density at high redshift provides a valuable constraint on the past star formation history and, with improved precision, may ultimately indicate whether there was sufficient star formation in the previous $\simeq 500$ -900 Myr to reionize the intergalactic medium.

We have demonstrated both the promise and limitations of this method by computing the comoving stellar mass density at $z \simeq 5$. Following the ideas discussed in Stark & Ellis (2006), we use the stellar mass density to constrain the amount of star formation at earlier times.

We detail our findings below.

1. We construct a sample of 25 spectroscopically confirmed $z \simeq 5$ objects in GOODS-S (14 of which are uncontaminated in the *Spitzer* data) to place a robust lower limit on the comoving stellar mass density. Fitting the SEDs of these objects to templates from Bruzual & Charlot (2003) populations synthesis models, we infer a total comoving stellar mass density of $1 \times 10^6 \text{ M}_\odot \text{ Mpc}^{-3}$.

2. We construct a sample of $z \simeq 5$ galaxies using the photometric redshifts of the GOODS-MUSIC catalog. After removing likely stellar and low- z contaminants, 196 objects remain in the sample. Computing the stellar mass from the 72 objects that are uncontaminated by nearby sources in the *Spitzer* data, we estimate a stellar mass density of $6 \times 10^6 \text{ M}_\odot \text{ Mpc}^{-3}$. Systematic uncertainty in the star formation history causes this value to be uncertain at the 30% level.

3. The total comoving stellar mass density ($6 \times 10^6 \text{ M}_\odot \text{ Mpc}^{-3}$) represents a lower limit for several reasons. First, robust stellar mass estimates are only attainable for reasonably massive galaxies; hence the estimates presented in this paper do not include the contribution from low-mass systems. Second, we require objects to be bright in the rest-frame UV (and hence actively forming stars) for selection into our sample. If there is a large population of quiescent galaxies at $z \simeq 5$, the total stellar mass density may be significantly higher than estimated. We estimate that the stellar mass density of massive galaxies is unlikely to exceed $1 \times 10^7 \text{ M}_\odot \text{ Mpc}^{-3}$.

4. The estimated comoving stellar mass density at $z \simeq 5$ suggests that current observations may be missing some star formation at $z > 5$. The missing star formation could, however, be accommodated by extincted star formation in LBGs currently seen at $z \simeq 6-10$ or in low-luminosity star-forming systems below the detection threshold of current observations. In the latter case, our results have important implications for searches for low luminosity SF systems at high redshift.

ACKNOWLEDGMENTS

D.P.S. is grateful for the hospitality of the School of Physics at the University of Exeter, where most of this work was completed. We thank Peter Capak, Johan Richard, Kevin Bundy, Adam Kraus, Elizabeth Stanway, Kuenley Chiu and Richard McMahon for enlightening conversations. We thank our anonymous referee for very insightful comments. A.B. gratefully acknowledges support from a Philip Leverhulme Prize. L.E. is supported by a PPARC studentship. This paper is based on observations made with the NASA/ESA Hubble Space Telescope, obtained from the Data Archive at the Space Telescope Science Institute,

which is operated by the Association of Universities for Research in Astronomy, Inc., under NASA contract NAS 5-26555. The *HST/ACS* observations are associated with proposals #9425 & 9583 (the GOODS public imaging survey). Spitzer VLT/FORS2 VLT/ISAAC We are grateful to the GOODS team for making their reduced images public – a very useful resource.

REFERENCES

- Beckwith, S., Somerville, R., & Stiavelli, M. 2003, STScI Newsletter, Vol 20. Issue 04
- Bertin, E., & Arnouts, S. 1996, A&AS, 117, 393
- Bouwens, R. J., Illingworth, G. D., Blakeslee, J., & Franx, M. 2006, ApJ, submitted
- Bouwens, R. J., Illingworth, G. D., Thompson, R. I., & Franx, M. 2005, ApJ, 624, L5
- Bouwens, R. J., et al. 2004, ApJ, 616, L79
- Bremer, M. N., Lehnert, M. D., Waddington, I., Hardcastle, M. J., Boyce, P. J., & Phillipps, S. 2004, MNRAS, 347, L7
- Bruzual, G., & Charlot, S. 2003, MNRAS, 344, 1000
- Bundy, K., Ellis, R. S., & Conselice, C. J. 2005, ApJ, 625, 621
- Bunker, A. J., Stanway, E. R., Ellis, R. S., & McMahon, R. G. 2004, MNRAS, 355, 374
- Chabrier, G. 2003, PASP, 115, 763
- Chary, R.-R., Stern, D., & Eisenhardt, P. 2005, ApJ, 635, L5
- Coleman, G. D., Wu, C.-C., & Weedman, D. W. 1980, ApJS, 43, 393
- Dickinson, M., et al. 2004, ApJ, 600, L99
- Dunlop, J. S., Cirasuolo, M., & McLure, R. J. 2006, submitted to MNRAS, astro-ph/0606192
- Egami, E., et al. 2005, ApJ, 618, L5
- Ellis, R., Santos, M. R., Kneib, J.-P., & Kuijken, K. 2001, ApJ, 560, L119
- Erb, D. K., Shapley, A. E., Steidel, C. C., Pettini, M., Adelberger, K. L., Hunt, M. P., Moorwood, A. F. M., & Cuby, J.-G. 2003, ApJ, 591, 101

- Eyles, L., Bunker, A., Ellis, R., Lacy, M., Stanway, E., Stark, D., & Chiu, K. 2006, ArXiv Astrophysics e-prints
- Eyles, L. P., Bunker, A. J., Stanway, E. R., Lacy, M., Ellis, R. S., & Doherty, M. 2005, MNRAS, 364, 443
- Fan, X., et al. 2006, AJ, 131, 1203
- Fazio, G. G., et al. 2004, ApJS, 154, 10
- Ford, H. C., et al. 2003, in Future EUV/UV and Visible Space Astrophysics Missions and Instrumentation. Edited by J. Chris Blades, Oswald H. W. Siegmund. Proceedings of the SPIE, Volume 4854, pp. 81-94 (2003)., ed. J. C. Blades & O. H. W. Siegmund, 81
- Giacconi, R., et al. 2002, ApJS, 139, 369
- Giavalisco, M., et al. 2004a, ApJ, 600, L103
- Giavalisco, M., et al. 2004b, ApJ, 600, L93
- Grazian, A., Fontana, A., C., D., Nonino, M., Salimbeni, S., E., G., S., C., & S., G. 2006, A&A, accepted
- Iwata, I., Ohta, K., Tamura, N., Ando, M., Wada, S., Watanabe, C., Akiyama, M., & Aoki, K. 2003, PASJ, 55, 415
- Kraus, A. L., White, R. J., & Hillenbrand, L. A. 2006, ArXiv Astrophysics e-prints
- Leggett, S. K., et al. 2002, ApJ, 564, 452
- Meurer, G. R., Heckman, T. M., & Calzetti, D. 1999, ApJ, 521, 64
- Mobasher, B., et al. 2005, ApJ, 635, 832
- Oke, J. B., & Gunn, J. E. 1983, ApJ, 266, 713
- Panagia, N., Fall, S. M., Mobasher, B., Dickinson, M., Ferguson, H. C., Giavalisco, M., Stern, D., & Wiklind, T. 2005, ApJ, 633, L1
- Papovich, C., Dickinson, M., & Ferguson, H. C. 2001, ApJ, 559, 620
- Papovich, C., Dickinson, M., Giavalisco, M., Conselice, C. J., & Ferguson, H. C. 2005, ApJ, 631, 101
- Peng, C. Y., Ho, L. C., Impey, C. D., & Rix, H.-W. 2002, AJ, 124, 266

- Pettini, M., Steidel, C. C., Adelberger, K. L., Dickinson, M., & Giavalisco, M. 2000, *ApJ*, 528, 96
- Salpeter, E. E. 1955, *ApJ*, 121, 161
- Schlegel, D. J., Finkbeiner, D. P., & Davis, M. 1998, *ApJ*, 500, 525
- Shapley, A. E., Steidel, C. C., Adelberger, K. L., Dickinson, M., Giavalisco, M., & Pettini, M. 2001, *ApJ*, 562, 95
- Shapley, A. E., Steidel, C. C., Erb, D. K., Reddy, N. A., Adelberger, K. L., Pettini, M., Barmby, P., & Huang, J. 2005, *ApJ*, 626, 698
- Sirianni, M., et al. 2005, *PASP*, 117, 1049
- Spergel, D. N., et al. 2006, *ApJ*, submitted
- Spergel, D. N., et al. 2003, *ApJS*, 148, 175
- Stanway, E. 2004, PhD Thesis
- Stanway, E. R., Bunker, A. J., & McMahon, R. G. 2003, *MNRAS*, 342, 439
- Stanway, E. R., McMahon, R. G., & Bunker, A. J. 2005, *MNRAS*, 359, 1184
- Stark, D. P., & Ellis, R. S. 2006, *New Astronomy Review*, 50, 46
- Stark, D. P., Ellis, R. S., Richard, J., Kneib, J. P., Smith, G. P., & Santos, M. R. 2007, *ApJ*, submitted
- Steidel, C. C., Adelberger, K. L., Giavalisco, M., Dickinson, M., & Pettini, M. 1999, *ApJ*, 519, 1
- Steidel, C. C., Giavalisco, M., Pettini, M., Dickinson, M., & Adelberger, K. L. 1996, *ApJ*, 462, L17
- van Dokkum, P. G., et al. 2006, *ApJ*, 638, L59
- Vanzella, E., et al. 2002, *A&A*, 396, 847
- Vanzella, E., et al. 2005, *A&A*, 434, 53
- West, A. A., Walkowicz, L. M., & Hawley, S. L. 2005, *PASP*, 117, 706
- Yan, H., Dickinson, M., Giavalisco, M., Stern, D., Eisenhardt, P. R. M., & Ferguson, H. C. 2006, *ArXiv Astrophysics e-prints*

Yan, H., et al. 2005, ApJ, 634, 109

Yan, H., & Windhorst, R. A. 2004, ApJ, 600, L1

Table 1. Photometric catalog of $z \simeq 5$ galaxies in GOODS-S Field

ID	RA (J2000)	Dec (J2000)	v	i'	z'	J	K_s	3.6 μm	4.5 μm	z_{phot}
44_2919	03 32 9.054	-27 43 51.85	27.58 \pm 0.16	26.02 \pm 0.08	25.65 \pm 0.07	25.37 \pm 0.26	25.50 \pm 0.44	24.01 \pm 0.09	24.29 \pm 0.14	4.590
42_3601	03 32 10.64	-27 50 29.15	26.83 \pm 0.08	25.69 \pm 0.06	25.60 \pm 0.07	26.04 \pm 0.42	25.37 \pm 0.37	24.93 \pm 0.20	25.41 \pm 0.43	4.480
33_4001	03 32 11.44	-27 47 38.63	27.88 \pm 0.18	25.95 \pm 0.06	25.77 \pm 0.07	25.43 \pm 0.31	25.46 \pm 0.71	24.00 \pm 0.09	24.31 \pm 0.17	4.720
33_4496	03 32 12.42	-27 47 2.483	27.83 \pm 0.20	26.35 \pm 0.10	26.21 \pm 0.12	26.35 \pm 0.59	26.03 \pm 0.98	>25.8	>25.4	4.480
33_4687	03 32 12.78	-27 48 2.599	27.47 \pm 0.11	26.15 \pm 0.07	25.96 \pm 0.08	25.48 \pm 0.26	25.58 \pm 0.62	24.29 \pm 0.10	24.95 \pm 0.23	4.590
34_4915	03 32 13.25	-27 43 8.289	27.90 \pm 0.22	26.32 \pm 0.10	26.16 \pm 0.11	25.93 \pm 0.41	25.85 \pm 0.68	25.59 \pm 0.41	>25.4	4.680
35_5207	03 32 13.88	-27 41 48.54	29.35 \pm 0.83	27.27 \pm 0.23	26.49 \pm 0.15	29.30 \pm 9.44	>25.3	25.88 \pm 0.61	>25.4	5.340
33_5533	03 32 14.49	-27 49 32.69	26.67 \pm 0.07	25.69 \pm 0.06	25.53 \pm 0.06	26.21 \pm 0.56	25.53 \pm 0.48	25.07 \pm 0.33	25.85 \pm 0.72	4.460
33_5986	03 32 15.35	-27 49 36.08	27.78 \pm 0.19	26.15 \pm 0.09	26.35 \pm 0.13	25.79 \pm 0.38	25.40 \pm 0.41	25.27 \pm 0.58	26.18 \pm 0.44	4.610
33_6438	03 32 16.17	-27 46 41.59	28.74 \pm 0.47	26.25 \pm 0.10	26.00 \pm 0.10	26.63 \pm 0.75	>25.3	25.16 \pm 0.22	26.04 \pm 0.64	5.080
33_6440	03 32 16.17	-27 48 19.42	27.83 \pm 0.20	26.39 \pm 0.11	26.25 \pm 0.13	25.71 \pm 0.33	25.00 \pm 0.38	24.88 \pm 0.15	25.28 \pm 0.31	4.700
33_6519	03 32 16.34	-27 48 31.99	27.87 \pm 0.21	26.06 \pm 0.08	26.13 \pm 0.11	>26.0	>25.3	25.79 \pm 0.31	26.19 \pm 0.68	4.490
33_6575	03 32 16.45	-27 46 39.24	29.45 \pm 0.89	26.49 \pm 0.12	26.11 \pm 0.11	25.90 \pm 0.39	25.08 \pm 0.41	24.22 \pm 0.09	25.00 \pm 0.25	5.210
32_6854	03 32 16.98	-27 51 23.17	27.41 \pm 0.14	25.62 \pm 0.05	25.70 \pm 0.08	25.97 \pm 0.44	24.48 \pm 0.19	23.97 \pm 0.07	24.44 \pm 0.16	4.550
35_6867	03 32 17.00	-27 41 13.71	26.89 \pm 0.08	25.38 \pm 0.04	25.13 \pm 0.04	24.92 \pm 0.23	24.37 \pm 0.24	23.43 \pm 0.04	23.82 \pm 0.08	4.590
32_8020	03 32 18.91	-27 53 2.746	27.77 \pm 0.19	25.13 \pm 0.03	24.49 \pm 0.03	24.74 \pm 0.13	24.06 \pm 0.13	22.73 \pm 0.02	22.74 \pm 0.03	5.550
31_8593	03 32 19.96	-27 54 58.98	28.64 \pm 0.56	26.84 \pm 0.21	25.83 \pm 0.11	25.50 \pm 0.34	25.59 \pm 0.45	24.66 \pm 0.11	25.23 \pm 0.26	5.320
31_9014	03 32 20.70	-27 55 36.14	26.70 \pm 0.10	25.67 \pm 0.08	25.72 \pm 0.10	25.99 \pm 0.54	24.99 \pm 0.26	24.08 \pm 0.07	24.32 \pm 0.12	4.520
33_9184	03 32 21.01	-27 49 59.16	27.23 \pm 0.12	26.03 \pm 0.08	26.16 \pm 0.11	26.67 \pm 0.63	>25.3	>25.8	>25.4	4.580
33_9338	03 32 21.28	-27 49 59.67	28.54 \pm 0.38	26.84 \pm 0.16	26.14 \pm 0.11	25.85 \pm 0.30	26.64 \pm 0.92	25.76 \pm 0.26	25.35 \pm 0.26	5.500
33_9677	03 32 21.82	-27 50 3.346	28.74 \pm 0.46	26.49 \pm 0.12	26.48 \pm 0.15	>26.0	25.48 \pm 0.31	25.56 \pm 0.28	>25.4	4.800
34_9738	03 32 21.93	-27 45 33.07	28.22 \pm 0.29	26.20 \pm 0.09	25.82 \pm 0.09	26.20 \pm 0.51	24.90 \pm 0.23	24.31 \pm 0.09	24.72 \pm 0.18	4.800
33_9812	03 32 22.02	-27 46 42.89	26.76 \pm 0.08	25.41 \pm 0.05	25.26 \pm 0.05	25.94 \pm 0.48	24.84 \pm 0.25	23.84 \pm 0.06	24.05 \pm 0.10	4.510
34_9822	03 32 22.03	-27 45 29.31	27.38 \pm 0.14	26.41 \pm 0.11	26.28 \pm 0.13	26.00 \pm 0.42	>25.3	25.30 \pm 0.22	25.42 \pm 0.33	4.570
33_10064	03 32 22.44	-27 47 46.17	28.58 \pm 0.40	26.64 \pm 0.14	26.34 \pm 0.13	26.46 \pm 0.77	25.57 \pm 0.47	24.86 \pm 0.13	25.22 \pm 0.27	5.020
32_10232	03 32 22.71	-27 51 54.40	27.90 \pm 0.25	26.14 \pm 0.10	25.68 \pm 0.08	25.58 \pm 0.28	25.03 \pm 0.24	24.27 \pm 0.08	24.82 \pm 0.16	5.050
33_10340	03 32 22.88	-27 47 27.56	26.64 \pm 0.07	24.94 \pm 0.04	24.84 \pm 0.04	24.55 \pm 0.13	24.59 \pm 0.16	23.75 \pm 0.05	24.01 \pm 0.10	4.440
31_10974	03 32 24.00	-27 54 59.79	27.51 \pm 0.16	25.46 \pm 0.05	24.73 \pm 0.03	24.56 \pm 0.16	24.89 \pm 0.25	25.39 \pm 0.41	25.88 \pm 0.66	5.380
32_11635	03 32 25.02	-27 50 24.49	29.10 \pm 0.56	27.13 \pm 0.18	26.05 \pm 0.09	25.61 \pm 0.24	25.42 \pm 0.30	24.68 \pm 0.13	24.67 \pm 0.17	5.430
33_13701	03 32 27.94	-27 46 18.57	26.37 \pm 0.06	25.18 \pm 0.04	25.22 \pm 0.05	25.09 \pm 0.21	24.44 \pm 0.15	24.02 \pm 0.10	24.13 \pm 0.13	4.480
34_14195	03 32 28.70	-27 42 28.95	28.11 \pm 0.21	26.23 \pm 0.08	26.03 \pm 0.08	26.82 \pm 0.84	>25.3	25.67 \pm 0.34	>25.4	4.840
22_15316	03 32 30.28	-27 49 22.01	28.04 \pm 0.25	26.47 \pm 0.12	25.88 \pm 0.09	26.30 \pm 0.47	>25.3	>25.8	>25.4	5.200
22_15851	03 32 31.07	-27 51 17.85	28.91 \pm 0.54	26.17 \pm 0.09	26.04 \pm 0.10	26.06 \pm 0.40	24.89 \pm 0.22	24.62 \pm 0.17	24.93 \pm 0.25	4.820
23_16055	03 32 31.37	-27 48 13.81	28.08 \pm 0.26	26.20 \pm 0.10	25.89 \pm 0.09	25.09 \pm 0.20	25.66 \pm 0.39	24.94 \pm 0.14	25.42 \pm 0.32	4.990
22_17535	03 32 33.69	-27 53 21.62	29.06 \pm 0.61	27.28 \pm 0.24	26.39 \pm 0.14	>26.0	>25.3	26.28 \pm 0.60	>25.4	5.360

Table 1—Continued

ID	RA (J2000)	Dec (J2000)	v	i'	z'	J	K_s	3.6 μm	4.5 μm	z_{phot}
23_17728	03 32 33.98	-27 48 2.043	27.61 \pm 0.17	26.10 \pm 0.09	25.90 \pm 0.09	25.74 \pm 0.29	24.52 \pm 0.13	24.08 \pm 0.07	24.24 \pm 0.11	4.470
23_18716	03 32 35.45	-27 49 35.20	29.41 \pm 0.60	26.63 \pm 0.10	26.35 \pm 0.09	25.71 \pm 0.28	25.94 \pm 0.49	25.12 \pm 0.22	25.91 \pm 0.56	4.930
22_19011	03 32 35.89	-27 52 44.02	27.78 \pm 0.19	26.51 \pm 0.12	26.27 \pm 0.12	26.92 \pm 0.85	>25.3	25.70 \pm 0.34	>25.4	4.740
24_19118	03 32 36.08	-27 44 3.942	27.28 \pm 0.12	26.07 \pm 0.08	25.75 \pm 0.08	24.80 \pm 0.12	25.22 \pm 0.26	24.38 \pm 0.13	25.01 \pm 0.27	4.550
23_19268	03 32 36.30	-27 49 52.79	27.44 \pm 0.14	26.03 \pm 0.08	25.86 \pm 0.09	25.36 \pm 0.21	24.70 \pm 0.16	23.96 \pm 0.09	24.56 \pm 0.18	4.510
24_19435	03 32 36.49	-27 43 53.46	28.52 \pm 0.37	26.93 \pm 0.17	26.43 \pm 0.14	25.83 \pm 0.31	25.93 \pm 0.55	25.01 \pm 0.19	25.59 \pm 0.42	4.620
25_19912	03 32 37.25	-27 42 2.570	28.47 \pm 0.35	26.42 \pm 0.11	26.00 \pm 0.10	25.81 \pm 0.32	>25.3	25.04 \pm 0.18	25.53 \pm 0.41	5.180
22_20159	03 32 37.62	-27 50 22.38	>29.5	27.18 \pm 0.22	26.24 \pm 0.12	25.37 \pm 0.20	25.54 \pm 0.36	24.64 \pm 0.14	24.66 \pm 0.17	5.510
22_20304	03 32 37.86	-27 52 59.10	27.43 \pm 0.15	26.47 \pm 0.12	26.25 \pm 0.13	>26.0	>25.3	25.68 \pm 0.45	25.92 \pm 0.57	4.520
23_20360	03 32 37.95	-27 47 11.05	27.39 \pm 0.13	25.80 \pm 0.07	26.21 \pm 0.12	>26.0	>25.3	24.93 \pm 0.19	>25.4	4.690
22_21669	03 32 40.08	-27 50 49.60	27.72 \pm 0.18	26.28 \pm 0.10	26.05 \pm 0.10	25.74 \pm 0.30	25.56 \pm 0.40	25.45 \pm 0.29	26.17 \pm 0.64	4.520
24_22091	03 32 40.85	-27 45 46.25	28.03 \pm 0.18	26.14 \pm 0.07	25.33 \pm 0.04	25.12 \pm 0.14	25.22 \pm 0.32	24.76 \pm 0.12	24.45 \pm 0.14	5.400
23_22354	03 32 41.34	-27 48 43.13	28.02 \pm 0.24	26.31 \pm 0.11	26.14 \pm 0.11	>26.0	26.02 \pm 0.62	24.72 \pm 0.13	25.46 \pm 0.33	4.530
25_22925	03 32 42.36	-27 41 14.87	27.38 \pm 0.21	25.94 \pm 0.13	25.41 \pm 0.09	26.10 \pm 0.62	24.65 \pm 0.36	24.12 \pm 0.09	24.77 \pm 0.21	5.010
24_23215	03 32 42.95	-27 43 39.65	29.16 \pm 0.67	26.68 \pm 0.14	26.09 \pm 0.11	>26.0	>25.3	25.94 \pm 0.59	25.84 \pm 0.63	5.200
24_23395	03 32 43.30	-27 43 10.59	28.73 \pm 0.45	26.14 \pm 0.09	26.25 \pm 0.12	25.60 \pm 0.32	>25.3	24.74 \pm 0.16	25.10 \pm 0.30	4.780
23_23515	03 32 43.53	-27 49 19.21	27.89 \pm 0.21	25.80 \pm 0.07	25.53 \pm 0.07	26.05 \pm 0.34	25.84 \pm 0.50	24.89 \pm 0.15	25.92 \pm 0.49	5.090
22_25323	03 32 47.58	-27 52 28.18	28.49 \pm 0.34	26.43 \pm 0.11	26.24 \pm 0.11	25.43 \pm 0.26	>25.3	25.43 \pm 0.29	>25.4	4.760
13_25544	03 32 48.14	-27 48 17.69	27.95 \pm 0.23	26.04 \pm 0.09	25.41 \pm 0.06	25.64 \pm 0.28	24.89 \pm 0.25	24.65 \pm 0.12	24.97 \pm 0.24	5.170
14_25620	03 32 48.33	-27 45 38.90	27.86 \pm 0.21	26.24 \pm 0.11	26.37 \pm 0.14	26.42 \pm 0.49	25.75 \pm 0.52	>25.8	>25.4	4.610
12_25696	03 32 48.53	-27 54 25.67	27.44 \pm 0.12	26.28 \pm 0.08	26.24 \pm 0.10	26.49 \pm 0.77	>25.3	24.89 \pm 0.20	25.63 \pm 0.45	4.530
12_25851	03 32 48.89	-27 52 43.17	27.75 \pm 0.18	26.49 \pm 0.12	26.39 \pm 0.14	>26.0	>25.3	>25.8	>25.4	4.540
12_25952	03 32 49.15	-27 50 22.52	28.24 \pm 0.29	26.04 \pm 0.08	25.30 \pm 0.05	25.27 \pm 0.19	25.52 \pm 0.39	25.20 \pm 0.18	25.54 \pm 0.33	5.360
12_26198	03 32 49.81	-27 50 22.75	28.23 \pm 0.28	26.42 \pm 0.10	26.12 \pm 0.10	25.58 \pm 0.27	25.35 \pm 0.35	25.94 \pm 0.41	26.22 \pm 0.65	5.110
12_26409	03 32 50.44	-27 50 39.64	>29.5	27.01 \pm 0.20	26.38 \pm 0.14	>26.0	>25.3	26.30 \pm 0.57	26.70 \pm 0.99	5.460
13_26480	03 32 50.63	-27 49 34.79	>29.5	26.83 \pm 0.16	26.36 \pm 0.14	>26.0	>25.3	>25.8	>25.4	5.220
13_26492	03 32 50.65	-27 47 15.18	26.80 \pm 0.09	25.84 \pm 0.08	25.64 \pm 0.07	26.26 \pm 0.49	>25.3	25.42 \pm 0.28	>25.4	4.430
12_26985	03 32 51.94	-27 52 8.494	27.46 \pm 0.15	26.04 \pm 0.09	25.95 \pm 0.09	26.19 \pm 0.58	>25.3	>25.8	>25.4	4.580
12_27749	03 32 54.05	-27 51 12.02	29.12 \pm 0.68	27.09 \pm 0.20	26.32 \pm 0.13	>26.0	>25.3	25.82 \pm 0.85	>25.4	5.500
12_28370	03 32 56.22	-27 51 51.29	27.81 \pm 0.20	26.33 \pm 0.10	26.17 \pm 0.11	>26.0	>25.3	25.01 \pm 0.21	>25.4	4.570
12_28389	03 32 56.29	-27 53 31.53	27.33 \pm 0.12	25.66 \pm 0.05	25.60 \pm 0.07	24.62 \pm 0.17	24.83 \pm 0.27	24.61 \pm 0.15	25.03 \pm 0.29	4.690
12_28728	03 32 57.68	-27 53 19.67	28.05 \pm 0.25	26.09 \pm 0.08	26.08 \pm 0.10	25.99 \pm 0.59	>25.3	24.99 \pm 0.21	25.26 \pm 0.32	4.930
12_28859	03 32 58.38	-27 53 39.59	26.41 \pm 0.05	25.54 \pm 0.04	25.62 \pm 0.06	>26.0	26.65 \pm 0.88	24.98 \pm 0.30	24.92 \pm 0.28	4.420
12_28917	03 32 58.66	-27 52 43.69	28.33 \pm 0.32	26.11 \pm 0.09	25.81 \pm 0.08	>26.0	24.98 \pm 0.33	25.05 \pm 0.20	25.94 \pm 0.64	4.840
12_28990	03 32 59.01	-27 53 32.22	27.47 \pm 0.13	25.55 \pm 0.05	25.20 \pm 0.04	25.13 \pm 0.21	24.42 \pm 0.17	23.39 \pm 0.06	24.07 \pm 0.13	4.860

Table 1—Continued

ID	RA (J2000)	Dec (J2000)	v	i'	z'	J	K_s	3.6 μm	4.5 μm	z_{phot}
12_29097	03 32 59.72	-27 52 2.582	29.20 \pm 0.73	26.31 \pm 0.10	25.67 \pm 0.07	>26.0	>25.3	24.05 \pm 0.11	24.66 \pm 0.25	5.170
12_29119	03 32 59.89	-27 52 56.42	28.53 \pm 0.40	26.70 \pm 0.15	26.29 \pm 0.13	>26.0	24.91 \pm 0.15	23.88 \pm 0.08	24.12 \pm 0.14	4.890

Table 2. Spectroscopically-confirmed $z \simeq 5$ galaxies in GOODS-S Field

ID	RA (J2000)	Dec (J2000)	Redshift	$v - i'$	$i' - z'$	Spitzer Confusion Class	Redshift Flag	Included in SED fitting
44_1543	03 32 5.258	-27 43 0.406	4.81	1.85	-0.09	4	A	N
35_4142	03 32 11.71	-27 41 49.59	4.91	1.79	0.17	3	C	Y
35_4244	03 32 11.92	-27 41 57.09	5.57	1.39	1.05	3/4	B	N
35_6626	03 32 16.55	-27 41 3.203	5.25	2.07	0.92	3	C	Y
35_6867	03 32 17.00	-27 41 13.71	4.41	1.54	0.11	1	B	N
33_7471	03 32 17.95	-27 48 17.01	5.40	1.82	1.16	4	C	N
32_8020	03 32 18.91	-27 53 2.746	5.55	2.60	0.57	1	A	Y
35_9350	03 32 21.30	-27 40 51.20	5.29	1.84	0.71	1	A	Y
34_9738	03 32 21.93	-27 45 33.07	4.78	2.00	0.28	3	C	Y
32_10232	03 32 22.71	-27 51 54.40	4.90	2.05	0.42	1	C	Y
33_10340	03 32 22.88	-27 47 27.56	4.44	1.60	0.00	1	B	Y
no_ACS_01	03 32 22.89	-27 45 20.99	5.12	C	N
33_10388	03 32 22.97	-27 46 29.09	4.50	1.65	0.03	3/4	C	N
34_11820	03 32 25.31	-27 45 30.85	4.99	3.55	0.45	2	B	Y
35_14097	03 32 28.56	-27 40 55.71	4.59	1.67	0.37	3	B	Y
35_14303	03 32 28.84	-27 41 32.70	4.80	1.79	0.02	4	B	N
no_ACS_02	03 32 28.93	-27 41 28.19	4.88	B	N
31_14602	03 32 29.29	-27 56 19.46	4.76	1.67	0.10	3	B	Y
22_15184	03 32 30.09	-27 50 57.72	5.08	0.39	-0.05	...	B	N
24_18073	03 32 34.48	-27 44 3.008	4.94	1.46	-0.12	3/4	C	N
22_20159	03 32 37.62	-27 50 22.38	5.51	1.89	1.28	3/4	A	N
22_21502	03 32 39.81	-27 52 58.09	5.54	1.63	1.03	4	C	N
24_21686	03 32 40.11	-27 45 35.49	4.77	1.62	0.16	3/4	B	N
21_23040	03 32 42.62	-27 54 28.95	4.40	1.85	0.41	3	C	Y
23_23051	03 32 42.65	-27 49 38.99	4.84	2.23	0.06	3	C	Y
no_ACS_03	03 32 43.15	-27 50 34.80	4.83	C	N
23_24305	03 32 45.23	-27 49 9.829	5.58	1.61	1.22	3/4	B	N
21_24396	03 32 45.42	-27 54 38.52	5.37	2.64	0.69	3	A	Y
22_25323	03 32 47.58	-27 52 28.18	4.75	2.01	0.11	3	C	Y
12_28085	03 32 55.08	-27 54 14.48	4.71	1.88	0.13	3/4	A	N

Note. — All magnitudes are in AB system. no_ACS_01, no_ACS_02, and no_ACS_03, were not detected with *ACS*. The *Spitzer* confusion classes have the following meanings: 1 = isolated and detected; 2 = isolated but undetected; 3 = confused, but Galfit may help ; 4 = hopelessly confused. Those sources with Spitzer confusion class '3/4' were deemed hopelessly confused after attempting (and failing) to subtract nearby sources with Galfit.

Table 3. Photometric Properties of $z \simeq 5$ spectroscopically-confirmed galaxies.

ID	z_{spec}	v	i'	z'	J	K_s	3.6 μm	4.5 μm
35_4142	4.912	27.22 \pm 0.11	25.51 \pm 0.05	25.26 \pm 0.05	25.19 \pm 0.22	25.09 \pm 0.35	25.11 \pm 0.27	25.65 \pm 0.54
35_6626	5.250	29.07 \pm 0.62	27.18 \pm 0.21	26.35 \pm 0.13	26.19 \pm 0.52	>25.4
35_6867	4.416	26.89 \pm 0.08	25.38 \pm 0.04	25.13 \pm 0.04	24.92 \pm 0.23	24.37 \pm 0.24	23.43 \pm 0.04	23.82 \pm 0.08
32_8020	5.554	27.77 \pm 0.19	25.13 \pm 0.03	24.49 \pm 0.03	24.74 \pm 0.13	24.06 \pm 0.13	22.73 \pm 0.02	22.74 \pm 0.03
35_9350	5.283	28.07 \pm 0.32	26.04 \pm 0.10	25.41 \pm 0.08	25.52 \pm 0.60
34_9738	4.788	28.22 \pm 0.29	26.20 \pm 0.09	25.82 \pm 0.09	26.20 \pm 0.51	24.90 \pm 0.23	24.31 \pm 0.09	24.72 \pm 0.18
32_10232	4.900	27.90 \pm 0.25	26.14 \pm 0.10	25.68 \pm 0.08	25.58 \pm 0.28	25.03 \pm 0.24	24.27 \pm 0.08	24.82 \pm 0.16
33_10340	4.440	26.64 \pm 0.07	24.94 \pm 0.04	24.84 \pm 0.04	24.55 \pm 0.13	24.59 \pm 0.16	23.75 \pm 0.05	24.01 \pm 0.10
34_11820	4.992	28.78 \pm 0.45	26.95 \pm 0.16	26.66 \pm 0.16	>26.0	25.63 \pm 0.46	>25.8	>25.4
35_14097	4.597	27.72 \pm 0.17	25.92 \pm 0.07	25.87 \pm 0.08	25.19 \pm 0.30	25.16 \pm 0.38
31_14602	4.760	26.76 \pm 0.09	25.04 \pm 0.04	24.88 \pm 0.04	22.64 \pm 0.02	22.55 \pm 0.02
21_23040	4.400	28.17 \pm 0.28	26.12 \pm 0.08	25.79 \pm 0.08	25.30 \pm 0.26	25.49 \pm 0.43	24.02 \pm 0.06	24.57 \pm 0.14
23_23051	4.840	28.31 \pm 0.31	26.04 \pm 0.08	25.86 \pm 0.09	26.19 \pm 0.38	25.87 \pm 0.50	24.93 \pm 0.14	25.12 \pm 0.23
21_24396	5.370	28.94 \pm 0.55	26.09 \pm 0.08	25.30 \pm 0.05	24.99 \pm 0.22	25.11 \pm 0.33	24.80 \pm 0.16	24.21 \pm 0.11
22_25323	4.758	28.49 \pm 0.34	26.43 \pm 0.11	26.24 \pm 0.11	25.43 \pm 0.26	>25.3	25.43 \pm 0.29	>25.4

Note. — The VLT mosaic does not cover the entire GOODS field. Those sources that are located off the edge of the VLT images denoted by an ellipsis.

Table 4. Modeling Results

Object	Star Formation History	$\log M_{\text{stellar}} (M_{\odot})$	Age (Myr)	E(B-V)	χ^2
35_4142	csf	9.34	161	0.00	2.11
35_6626	70	9.32	143	0.00	0.26
35_6867	100	10.37	360	0.01	1.77
32_8020	300	11.16	905	0.00	2.90
35_9350	csf	9.33	255	0.00	0.57
34_9738	100	10.13	360	0.00	1.37
32_10232	70	10.06	255	0.01	2.22
33_10340	100	11.28	18	0.24	1.82
35_14097	200	9.93	255	0.05	0.04
31_14602	300	11.10	1015	0.00	1.79
21_23040	burst	8.43	1	0.53	2.24
23_23051	100	9.86	286	0.00	0.47
21_24396	burst	8.40	9	0.17	0.21
22_25323	burst	8.43	3	0.32	0.61

Note. — In the star-formation history column, 'csf' corresponds to constant star formation, while the numbers (e.g 70, 100) correspond to the exponential decay constant (in Myr) for an exponentially-declining star formation history.

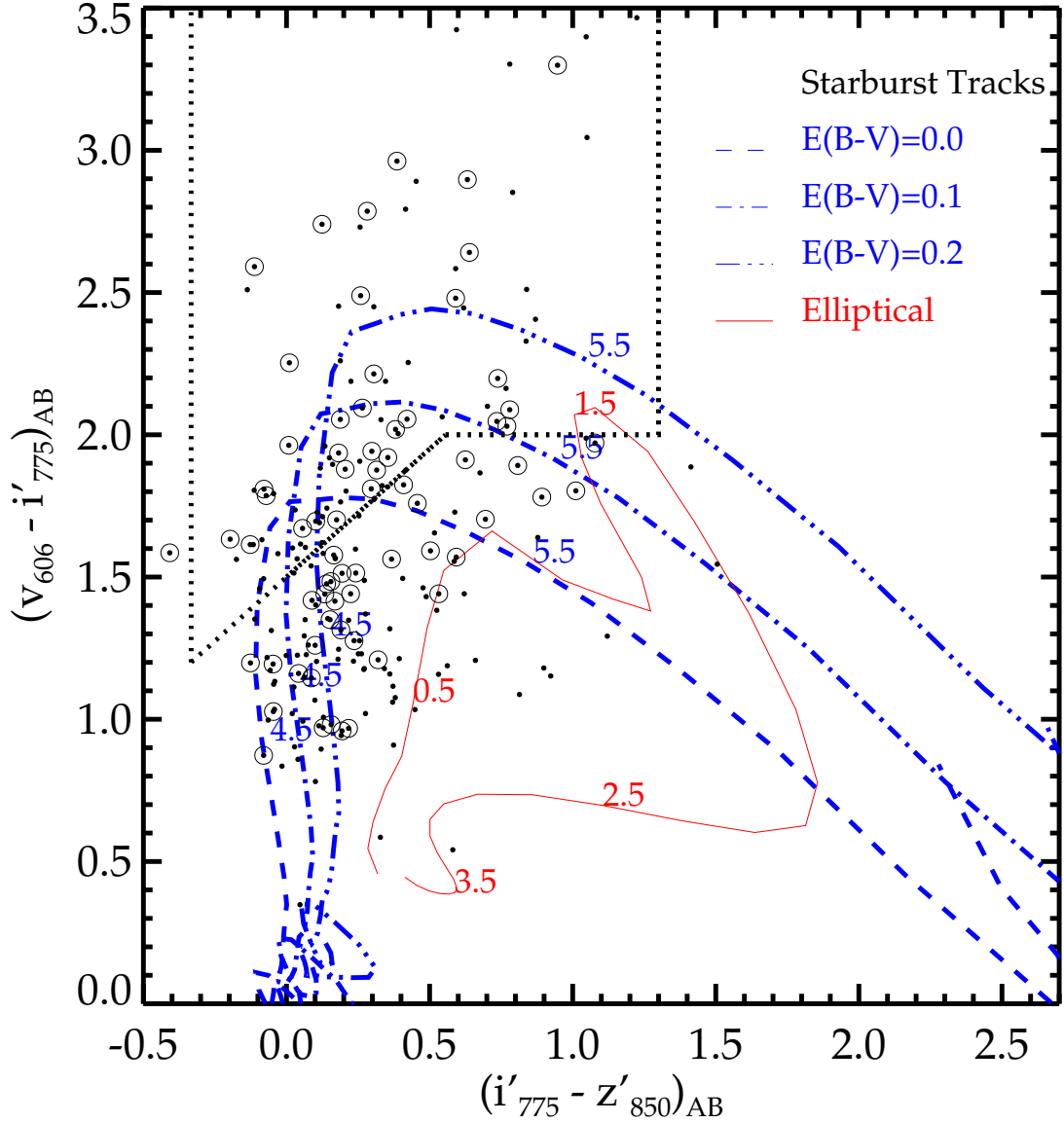


Fig. 1.— $(v_{606W} - i'_{775W})$ vs. $(i'_{775W} - z'_{850LP})$ colors of $z \simeq 5$ candidates in GOODS-S. We construct a sample of 214 objects with photometric redshifts between $4.4 < z < 5.6$ from the GOODS-MUSIC catalog (solid black circles). After removing stellar contaminants, low- z interlopers, and objects blended in Spitzer images, 72 objects with $z'_{850LP} < 26.5$ remain; these objects are marked with an additional circle. Although many objects in the sample fall just outside of the v -band dropout selection window used by Giavalisco et al. (2004a) to select $z \simeq 5$ galaxies (demarcated by dotted line), redshift tracks generated from starburst templates from Bruzual & Charlot (2003) illustrate that their rest-frame UV colors are consistent with the $z \simeq 5$ interpretation. These tracks assume an age of 100 Myr and a constant star formation rate with $E(B-V)=0.0, 0.1, 0.2$ (blue dashed line, dashed-dotted, dashed-triple-dotted, respectively). Redshifting an elliptical galaxy template (Coleman et al. 1980) to $z=0-4$ (red solid line), we see that old galaxies at $z \simeq 1.5$ could contaminate our sample.

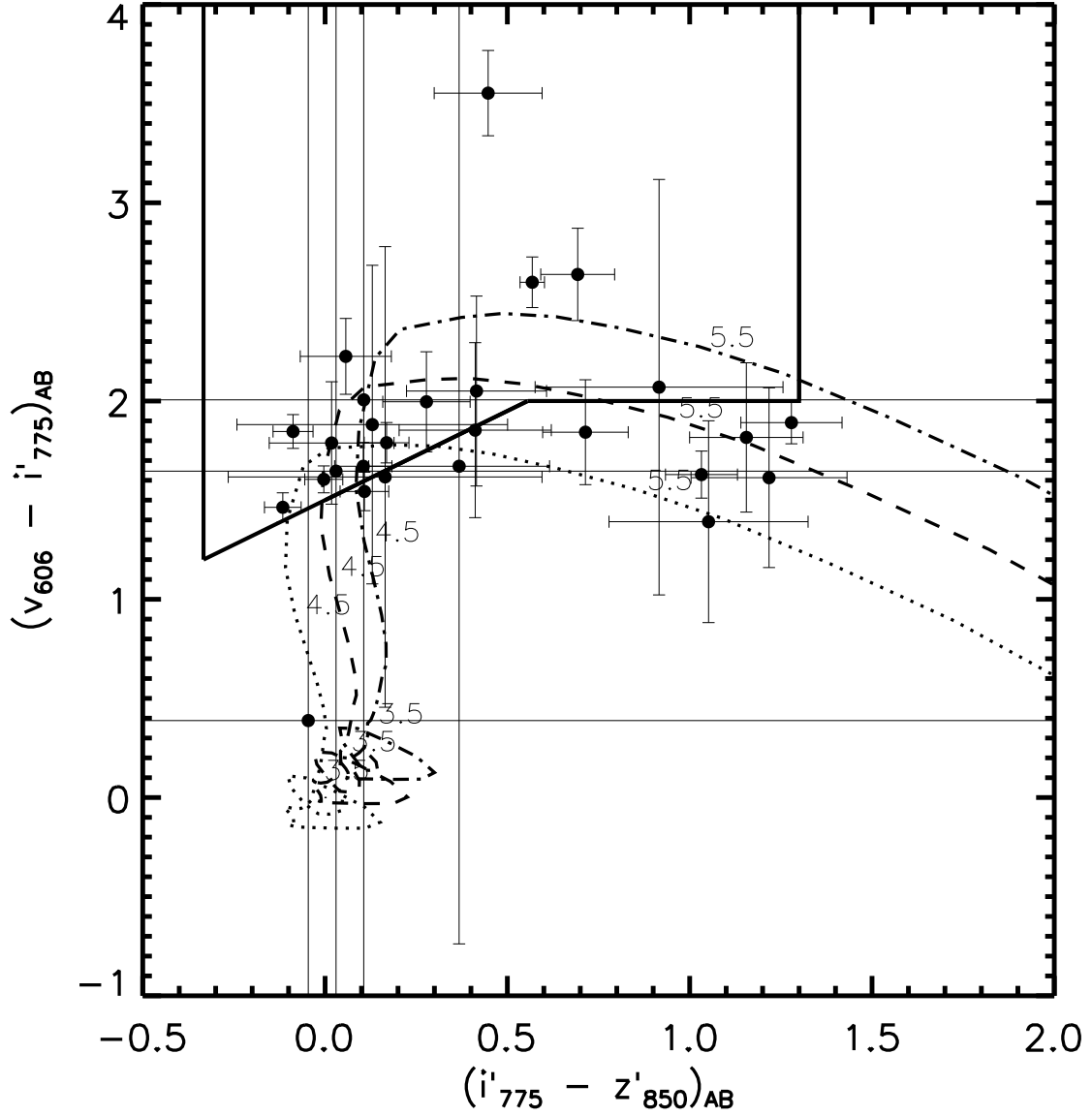


Fig. 2.— $(v_{606W} - i'_{775W})$ vs. $(i'_{775W} - z'_{850LP})$ colors of 30 galaxies with FORS2/VLT spectroscopic redshifts of $4.4 < z < 5.6$. The v -drop selection window described in Giavalisco et al. (2004a) is overlaid with a solid line. Starburst redshift tracks are identical to those described in Figure 1. Removing objects that either do not satisfy the magnitude limit of $z'_{850LP} < 26.5$ or do not have the rest-frame UV colors expected for a $z \simeq 5$ LBG leaves a sample of 25 objects.

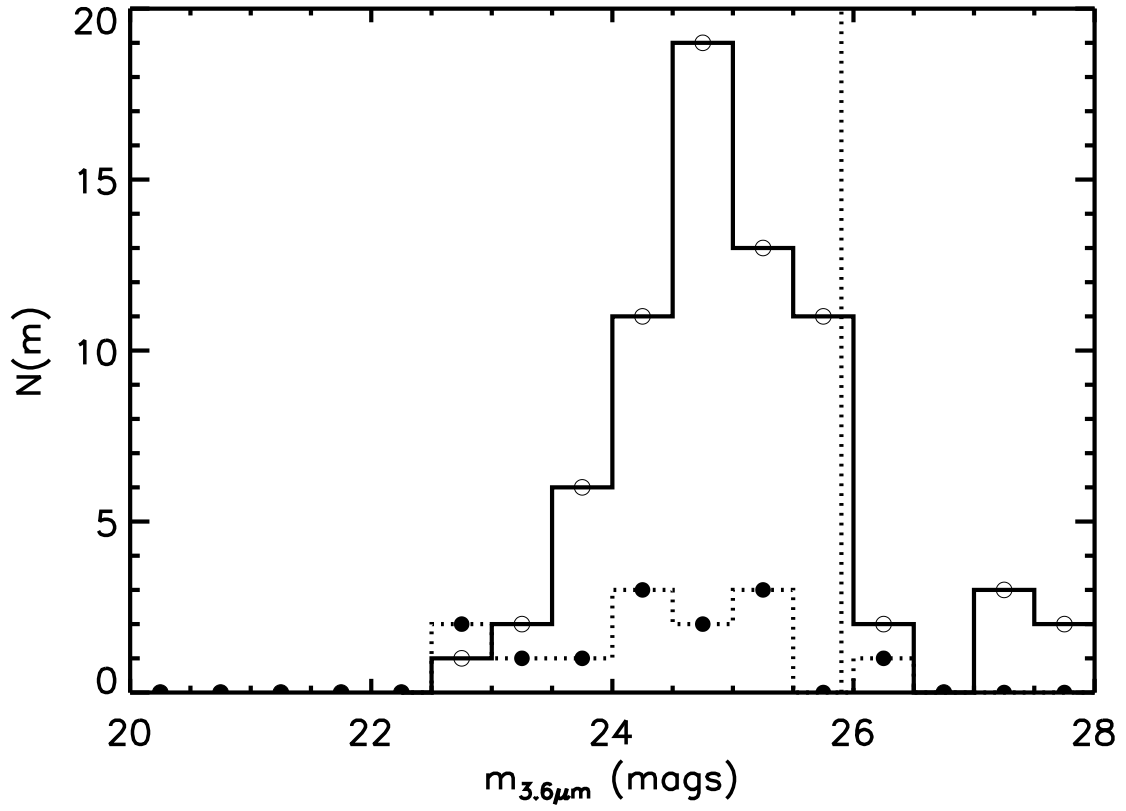


Fig. 3.— Distribution of IRAC 3.6 μm AB magnitudes for 72 photometrically- selected $z \approx 5$ candidates (open circles) and 14 spectroscopically-confirmed $z \approx 5$ galaxies (closed circles). The spectroscopic sample contains a larger relative fraction of Spitzer bright objects.

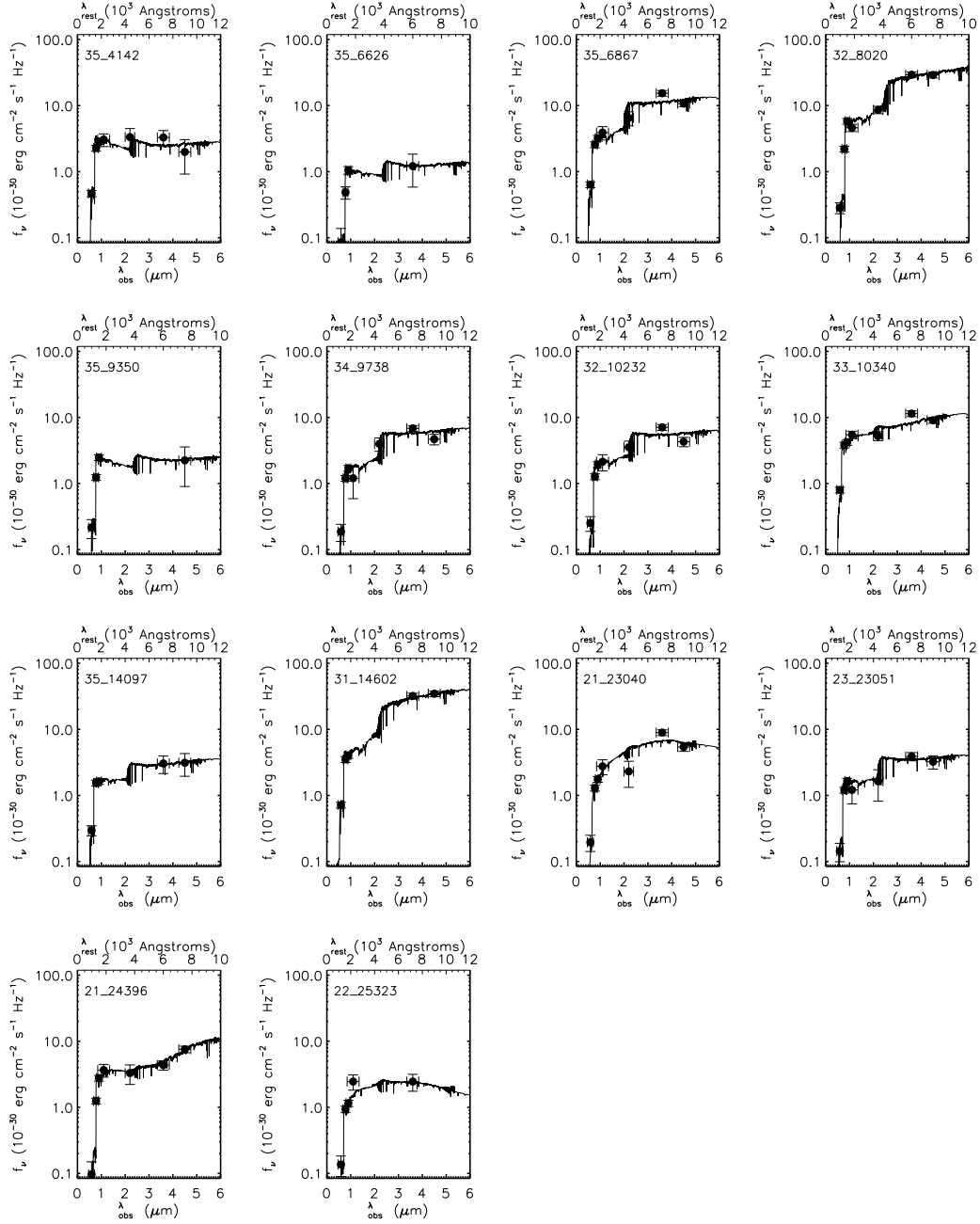


Fig. 4.— Observed and best-fit model Bruzual & Charlot (2003) SEDs of 15 spectroscopically-confirmed $z \simeq 5$ galaxies in GOODS-S. Best-fit model parameters are presented in Table 4. Three objects (32_8020, 31_14602, and 33_10340) have inferred stellar masses above $10^{11} M_\odot$, and an additional three objects have inferred stellar masses greater than $10^{10} M_\odot$.

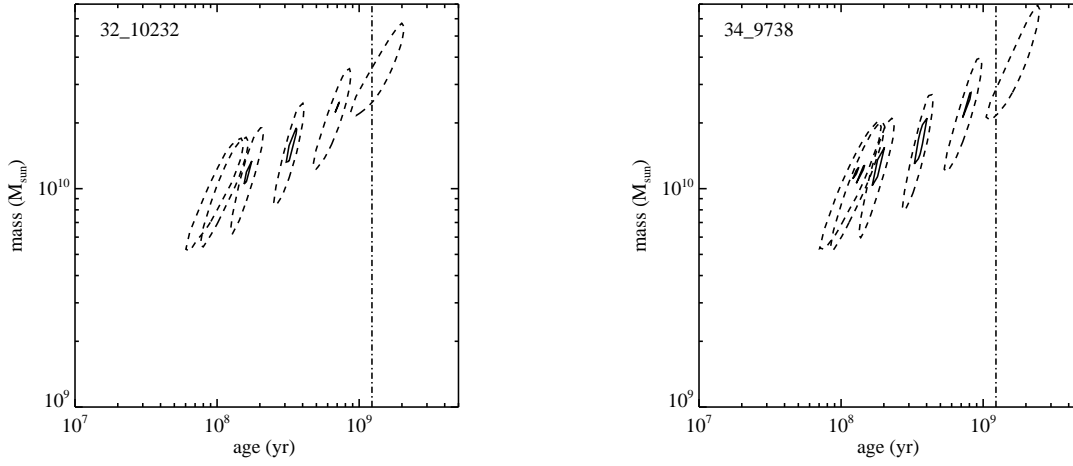


Fig. 5.— Confidence intervals for inferred stellar mass versus age for two objects from the spectroscopically-confirmed $z \simeq 5$ objects in GOODS-S. The ellipses are different assumed star formation histories, ranging from an initial burst to continuous star formation via a range of exponentially-decaying star formation histories. Contours are 68% confidence (solid line) and 95% confidence (dashed line) corresponding to $\Delta\chi^2_{\text{reduced}} = 1, 4$ (respectively), where $\Delta\chi^2_{\text{reduced}} = \chi^2_{\text{reduced}} - \chi^2_{\text{reduced,min}}$. The vertical dashed-dotted line at the right of each plot denotes the age of the universe at the source’s redshift. Solutions to the right of this line are ruled out. The typical 68% confidence uncertainties in the stellar mass are 30-50%.

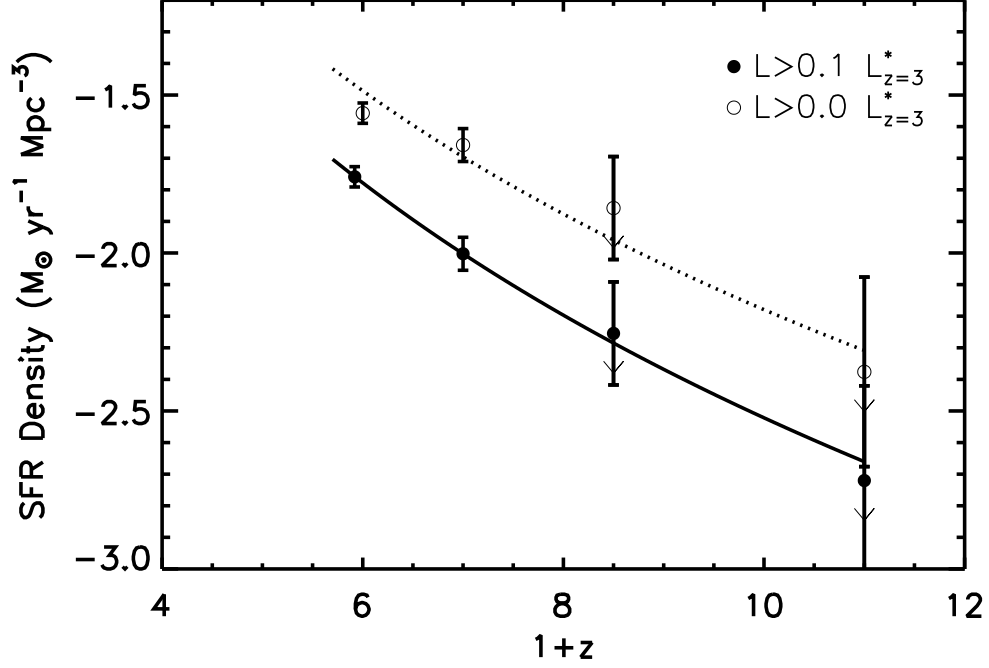


Fig. 6.— Comoving star formation rate density as a function of redshift, assuming no extinction. The star formation rate densities are derived from Giavalisco et al. (2004) at $z = 5$, Stanway (2005) and Bouwens et al. (2006) at $z = 6$, Bouwens et al. (2005) at $z = 7.5$, and Bouwens et al. (2005) at $z = 10$. The solid circles represent the star formation rate densities achieved by integrating the derived luminosity function down to $0.1 L_{z=3}^*$. Integrating the luminosity function down to zero luminosity (open circles) assuming a faint-end slope of $\alpha = -1.73$ adds an additional factor of 2.3 to the star formation rate density. The evolution of the star formation rate density with redshift is well fit by a $(1+z)^{-3.3}$ parameterization over $5 < z < 10$.

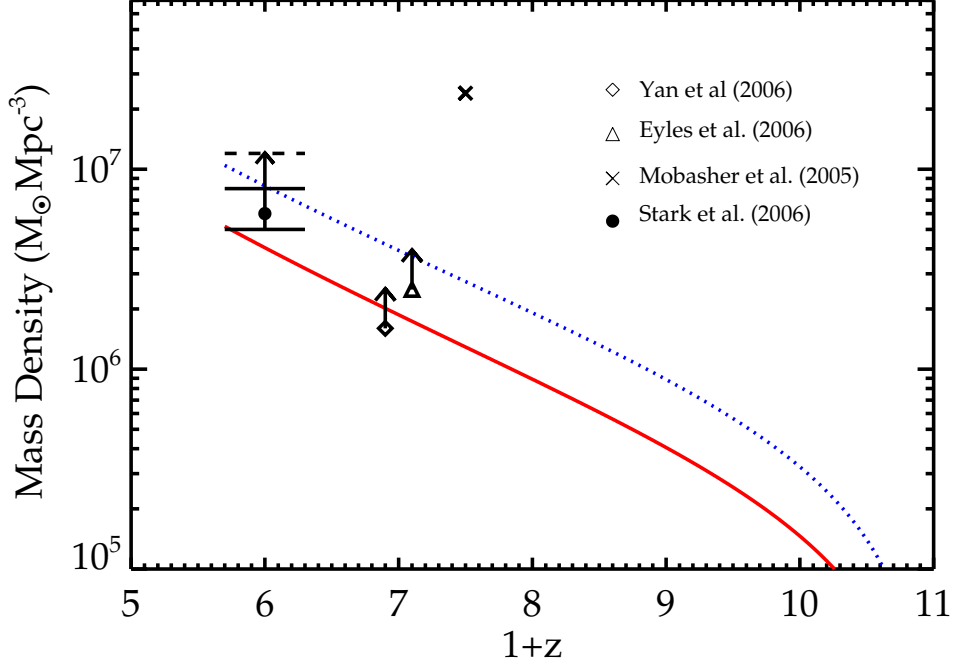


Fig. 7.— Comparison of stellar mass density at $z \simeq 5-10$ derived from spectral energy distributions of galaxies in GOODS-S with that derived from integrating the observed star formation rate density at $z \simeq 5-10$ integrated down to $0.1 L_{z=3}^*$ (solid line) and zero luminosity (dotted line) assuming a faint-end slope of $\alpha = -1.73$. The filled solid circle with the upward arrow corresponds to the stellar mass density derived from spectroscopically-confirmed galaxies in GOODS-S ($1 \times 10^6 M_\odot$) whereas the solid filled circle corresponds to the stellar mass density from the photometric sample ($6 \times 10^6 M_\odot$). We estimate that the stellar mass density may be as high as $1 \times 10^7 M_\odot \text{ Mpc}^{-3}$ (solid horizontal line) depending on the contribution from undetected sources. We also include previous estimates of the stellar mass density at $z > 5$ from Yan et al. (2006) (diamonds), Eyles et al. (2006) (triangle), and Mobasher et al. (2005) (cross). The Yan et al. (2006) and Eyles et al. (2006) symbols are offset slightly from $z = 6$ for clarity. The large stellar mass density at $z \simeq 5$ inferred from this study suggests that a significant amount of star formation is hidden by dust or has yet to be located, perhaps lying at higher redshift or in intrinsically faint systems.